Behavior of Brittle Materials Under Dynamic Loading

G. I. Kanel
Edited by S. J. Bless and A. M. Rajendran

Institute for Advanced Technology
The University of Texas at Austin

January 2000

IAT.R 0219

DTIC QUALITY INSPECTED 4

20010215 106

REPORT DOCUMENTATION PAGE

Form Approved
OMB NO. 0704-0188

1. AGENCY USE ONLY (Leave blank)	2. REPORT DATE	3. REPORT TYPE AND DATES COVERED
	January 2000	Technical Report

4. TITLE AND SUBTITLE

Behavior of Brittle Materials Under Dynamic Loading

5. FUNDING NUMBERS

Contract # DAAA21-93-C-0101

6. AUTHOR(S)

G. I. Kanel
Edited by S. J. Bless and A. M. Rajendran

7. PERFORMING ORGANIZATION NAME(S) AND ADDRESS(ES)

Institute for Advanced Technology
The University of Texas at Austin
3925 W. Braker Lane, Suite 400
Austin, TX 78759-5316

8. PERFORMING ORGANIZATION REPORT NUMBER

IAT.R 0219

9. SPONSORING / MONITORING AGENCY NAME(S) AND ADDRESS(ES)

U.S. Army Research Laboratory
ATTN: AMSRL-WM-B
Aberdeen Proving Ground, MD 21005-5066

10. SPONSORING / MONITORING AGENCY REPORT NUMBER

11. SUPPLEMENTARY NOTES

The view, opinions and/or findings contained in this report are those of the author(s) and should not be considered as an official Department of the Army position, policy, or decision, unless so designated by other documentation.

12a. DISTRIBUTION / AVAILABILITY STATEMENT

Approved for public release; distribution unlimited.

12b. DISTRIBUTION CODE

A

13. ABSTRACT (Maximum 200 words)

Dynamic loading of brittle materials is related to many applications, including explosive excavation of rocks, design of ceramic armor, meteor impact on spacecraft windows, particle damage to turbine blades, etc. When brittle materials are exposed to impact or explosive loading, inelastic deformation, fracture, and fragmentation occur under conditions of three-dimensional stress, where at least one stress component is compressive. Unlike fracture and fragmentation of brittle materials under tensile loading, response to compression is far from understood. Rapid application of loads can also introduce rate dependencies which make the analysis even more complicated. This review report is mainly focused on compressive failure. We have collected, reviewed, and assessed information on the behavior and properties of brittle materials that are of greatest current interest, namely polycrystalline ceramics, glasses, and rocks.

14. SUBJECT TERMS

inelastic deformation; fracture toughness; high strain rates; polycrystalline, dilatancy; microcracks; macroscopical faults; crack size; friction; shock/particle velocity; Hugoniot elastic limit (HEL); spall fracture/spallation; split Hopkinson pressure bar dynamic compression technique; VISAR laser Doppler velocimeter

15. NUMBER OF PAGES

56

16. PRICE CODE

17. SECURITY CLASSIFICATION OF REPORT	18. SECURITY CLASSIFICATION OF THIS PAGE	19. SECURITY CLASSIFICATION OF ABSTRACT	20. LIMITATION OF ABSTRACT
Unclassified	Unclassified	Unclassified	UL

Table of Contents

List of Figures

List of Tables

BEHAVIOR OF BRITTLE MATERIALS UNDER DYNAMIC LOADING

Written by G.I. Kanel[1]
Edited by S.J. Bless[2] and A.M. Rajendran[3]

[1]Russian Academy of Science
[2]Institute for Advanced Technology, University of Texas at Austin
[3]U.S. Army Research Laboratory, Aberdeen Proving Ground

1. INTRODUCTION

Areas of interest.

The interest in behavior of brittle material under dynamic loading is related to many applications, including explosive excavation of rocks, design of hard ceramic armors, meteorite impacts on spacecraft windows, impacts of condensed particles on turbine blades, et cetera. When impact or explosive attack happens, inelastic deformation, fracture, and fragmentation occur under conditions of three-dimensional stress, where at least one stress component is compressive. In this paper, we'll be most interested in the fracture properties of brittle materials under compression. One should say that, while the fracture and fragmentation of brittle materials under tension is more or less clear, their response to compression is less completely understood. The rapid application of load can also introduce rate dependencies which make the problem more complicated.

Features of ductile and brittle response.

Many definitions exist for ductile and brittle behavior of solid materials. Material failure refers to a condition in which a substance loses all or most of its ability to support shear loads. Phenomenologically, brittle response is associated with the failure without significant plastic deformation, while ductile response is associated with large plastic deformation which not necessary is completed by a failure. Microscopically, plastic deformation occurs through microshears produced by dislocation motion and is not associated with an appearance of cracks or other discontinuities. The plastic deformation does not influence the matter density. Brittle behavior, in contrast, is accompanied with nucleation and growth of one or numerous cracks. Tensile strength of brittle materials is usually much less than the compressive strength.

Griffith, 1921, originally explained the low tensile strength in terms of an inequality between the rate at which elastic energy is released and the rate at which surface energy is absorbed, as a flaw or crack extends within the material. This approach works reasonably well for brittle materials while for ductile materials the surface energy should include additionally the work of plastic deformation in the vicinity of growing flaws to agree with observations.

Greater work that has to be spent to increase the flaw surface means greater resistance to crack growth. For brittle materials this work is two orders of magnitude less than for ductile materials.

Brittle fractures nucleate and grow as a result of stress concentrations. However, the stress required to cause a crack to advance is a function of crack size. The main parameter which controls the fracture by a growing single crack is the fracture toughness, K_{ic}, which is a critical value of the stress intensity factor. The stress intensity factor is

$$K_I = \sigma \cdot f_I \cdot (\pi l)^{1/2},$$

where σ is normal tensile stress, l is the crack length, and geometrical parameter f_I accounts for the specimen and load geometry. Thus the stress intensity factor characterizes the stress field near the crack tip and does not depend on the crack size. The fracture toughness is determined by measurements. For hard brittle materials, it is by one or two orders of magnitude less than for ductile materials.

Qualitatively, the ductile and brittle inelastic deformations are illustrated in Figure 1. The shape of a body should change in response to application of a non-hydrostatic stress field. Above the elastic limit, inelastic deformation changes the form by shearing along inclined slip planes. In isotropic media the slip planes are inclined by 45° to the principal stress directions. Fig. 1a shows a model of a body which consists of a pile of plates. When a tensile or compressive force is applied along the model axis, the plates slide relative to one another, as shown in Fig. 1b, and in this way the shape of the body is changed. During the sliding the plates rotate relative to their initial orientations, so any straight line within the body which does not coincide with a sliding plate becomes kinked. In crystalline solids the sliding is realized through a movement of dislocations. However, simple sliding along parallel planes and in one direction is really observed only for some highly anisotropic single crystals, such as zinc. For crystals with a high lattice symmetry and for polycrystalline ductile solids, many sliding planes with different orientations are activated more or less simultaneously (Fig. 1c). As a result, the global shear is accommodated by sliding along many planes and in many directions, and plastic deformation is macroscopically homogeneous. Moreover, with uniformly distributed gliding planes of opposite slopes, plastic deformation may proceed without rotations of material blocks.
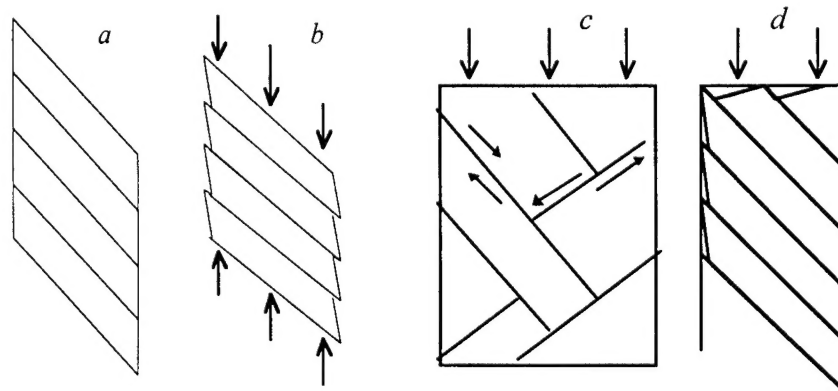
Fig. 1. Simplified models of inelastic deformation.

Hard solids with covalent-ionic interatomic bonds which are the subjects of our interest have a lower crystalline symmetry, higher Peierls energy barriers to dislocation motion, and a lower number of crystalline planes where dislocations may glide. In the model shown in Fig. 1, the sliding along optimally oriented planes starts when applied force becomes high enough, but it is not accommodated by an opposite sliding. If such a sliding is stopped inside the body, for example, by the grain boundary, it should result in opening voids or cracks, as shown in Fig. 1d. It is hardly possible that such cracks may appear in the planes which are perpendicular to the axis of compression, but it can be possible when the crack planes are parallel to the compression direction. It is natural to suppose also that the lateral stress or confining pressure should hinder the axial crack opening.

Open cracks and other voids in solids may appear only under tensile stresses. It is known that even when applied stress is wholly compressive, the local stress may become tensile at certain points at nonuniformities (McClintock and Argon 1966), and hence cracks may appear to grow in response to this local tensile stress. Based on Inglis' solution of the stress distribution around an elliptical hole in a plate (and assuming that the isotropic material contains cracks of all directions and that the maximum crack length), as well as the radius of curvature at the tip of the crack, is the same for cracks of all orientations, Griffith, 1924, derived a fracture criterion for biaxial stress conditions. He assumed that fracture occurs when the highest local tensile stress at the longest crack of the most dangerous orientation reaches a fixed critical value. According to the Griffith's criterion, fracture under biaxial stress occurs when

$$(\sigma_1 - \sigma_2)^2 + 8K(\sigma_1 + \sigma_2) = 0,$$

where σ_1, σ_2 are principal stresses, K is a material constant which is assumed to be ordinary tensile stress for uniaxial stressing. The cracking leads to irreversible loss in the resistance to deformation.

One should say that no absolutely brittle or absolutely ductile materials exist. Depending on the stress state and the loading conditions, a response of almost all solids can be brittle or ductile. However, while most ductile materials may form cracks, in stressed states approaching 3-D tension, most brittle materials may be deformed in a ductile manner only under conditions of high pressure. In fact, any solid material should exhibit ductility under loading conditions which suppress the cracking and create enough high shear stresses in the body.

Cracks are nucleated at non-uniformities within the body which are able to modify the stress field in such a way that some limited region with tensile stress component appear. Ceramics, rocks, and other non-homogeneous brittle materials contain numerous such damage nucleation sites which are more or less uniformly distributed through the body volume. In homogeneous glasses and single crystals, microdefects are concentrated mostly on the surfaces. As a result, a failure in such homogeneous materials propagates from the surface into the body volume. The different distributions of damage nucleation sites may influence the overall behavior of the brittle materials, especially at high strain rates. Whereas the response of each elementary volume of rock or ceramic materials is determined only by the applied stress and the

stress history, in the case of homogeneous brittle solids, we should account for whether or not the failure process propagating from the body surface has approached this elementary volume.

High strain rate measurements.

Measurements of mechanical properties of materials at high strain rates are mostly carried out using Hopkinson bars, plate impact, and bar impact techniques. In the latter two cases, the measurements are based on an analysis of the waves that propagate away from the impact loading plane. In the impact tests, the impact plane is loaded to failure, and the ensuing elastic wave has an amplitude equal to the elastic limit of the material for the specimen geometry. The bar impact technique realizes the one-dimensional stress conditions (e.g., unconfined compression), while plate impact experiments generate shock waves in one-dimensional strain. As a rule, shock-wave experiments provide information about bulk properties of the matter. It is assumed that the response of each volume element in the body is the same and depends only on its local state. The achievable strain rate range for shock-wave experiments is $\sim 10^4$ to 10^7 s^{-1}. In bar impact experiments, the state of the lateral specimen surface may contribute to the overall response, but it is usually assumed that the response of each cross section of the rod sample is similar. The modern Hopkinson bar technique is used to test materials at strain rates up to $\sim 10^4$ s^{-1} under different loading conditions. The technique provides information on properties of the sample as a whole.

Because of important applications, the behavior of brittle materials under intense dynamic loading is subjected to active studying. However, the qualitative and quantitative information that has been obtained is scattered over numerous publications and often is contradictory. The goal of this paper is to collect, review and assess information on the brittle materials that are of greatest current interest, namely polycrystalline, ceramics, glasses, and rocks.

2. GENERAL BEHAVIOR OF BRITTLE MATERIALS UNDER COMPRESSION

Microcracks and macroscopical faults.

A general behavior of brittle material and mechanisms of their inelastic deformation under compression was widely investigated for rocks. For more detailed information and review, the papers by Bombolakis, 1973, and Kranz, 1983, are recommended. Brittle failure is characterized by the appearance of one or a multitude of discrete discontinuities, which can range from a single crack to any degree of fracturing. Faults and other macroscopic fractures appear to form in brittle materials after attainment of the ultimate compressive stress, which is called the failure stress. A general fracture is preceded by microcracking, which starts in rocks when the maximum stress becomes one-third to two-thirds the failure stress. Orientations of these microcracks are predominantly within 10° of the applied load in uniaxially stressed rock. There appears to be a tendency for more of the observed trace orientations to be at higher

angles to the maximum applied stress direction at higher confining pressures (Wawersik and Brace 1971), although re-examination by Tapponier and Brace, 1976, at higher space resolution showed that these so-called 'shear cracks' may actually consist of axial arrays. Crack densities increase as macroscopic deviatoric stress increases above the threshold level at which microcracking started. In the post-failure region of compression, the rock samples collapse violently soon after reaching the failure stress. The load-carrying capacity typically drops rapidly to a low value.

Cracks are produced when the local tensile stress exceeds the local tensile strength. Microcracks, like other voids, may nucleate and grow only when at least the principle stress is tensile. Rocks and other brittle solids, by their nature, contain numerous flaws, cavities, inclusions, and other inhomogeneities. Local tensile stress may be created by stress concentrations at grain boundary contacts, around microcracks and cavities in the incident materials, as a result of twin lamellae interactions with grain boundaries and other twins, kink bands, or, in a larger scale, as a result of grain rotations and translations. A confining pressure strongly affects the strength and inelastic behavior of the rocks. At high values of hydrostatic stress, rocks deform by plastic mechanisms such as twining and gliding. Compressive failure of a brittle solid containing a distribution of flaws is illustrated in Figure 2.
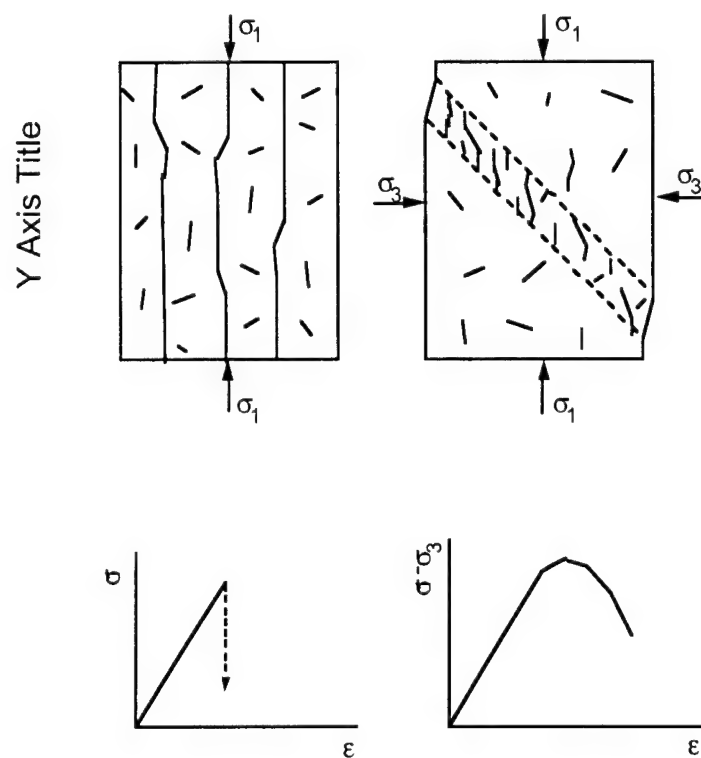
Fig. 2. Compressive failure of a brittle solid containing a distribution of flaws (left-axial splitting, right-shear fault).

5

Macroscopic through-going fracture in rock under compression is a result of the coalescence of many microcracks. As deviatoric stress increases and rock failure is approached, the microcrack population changes spatially from random to locally intense zones of cracking. Scholz, 1968, observed for a Westerly granite rapid acceleration in the microseismic activity within a few percent of the failure stress and distinct clustering of microfractures in a single inclined plane coincident with the eventual fault plane. The localization may accompany the formation of columns of rock material bounded by long cracks. Post-failure examinations of microcracks associated with the fracture indicate the density is very high in the fault region and dies off rapidly to the background level a few grains away. (The references have been collected by Kranz, 1983.)

Contrary to ductile materials, the fracture of rock specimens under one-dimensional stress conditions, or at relatively low confining pressure, often occurs by axial splitting or slabbing. For greater confining pressures, failure occurs by shear faulting at an angle less than 45° to the loading axis. The macroscopic faults develop out of multiple sources. The sources appear to be highly crushed regions which are traversed by long cracks. However, details concerning the onset and growth of the faults are still poorly understood.

The deviator stresses at which microcracking starts or failure occurs increase as the confining pressure increases. At some high pressure, a transition from brittle to ductile response occurs. The transitions between damage accumulation, structural failure and ductile response of a test specimen are often not sharp. It is better to speak of dominating mechanisms: below some pressure, brittle fracture dominates, while above, the transition ductile flow dominates. For example, Hockey, 1971, using transmission electron microscopy, has found extensive evidence of both slip and twinning in alumina at room-temperature indentation. Chan and Lawn, 1988, also observed basal twinning and pyramidal slip from indentation deformation of sapphire. These shear processes operated close to the cohesive limit. The factor which permits plastic flow under an indentor is the intense confining pressure induced within elastic surround. Heard and Cline, 1980, observed that failure followed immediately after essentially elastic deformation of Al_2O_3, AlN, and BeO when the confining pressure was low. The failure occurred by macroscopic shear on fault planes oriented at about 30° to the compression axes, while the rest of the material contained numerous axial microcracks. At a confining pressure > 0.5 GPa, the dominant deformation mechanism of BeO and AlN became intracrystalline slip by dislocation motion, with attendant pile-up at grain boundaries. These ceramics exhibit an increasing ductility when the confining pressure arises above the brittle-ductile transition. Hard alumina remains brittle at confining pressures at least up to 1.25 GPa. The ultimate compressive strength of ceramics increases rapidly with pressure growth below the brittle-ductile transition; above this threshold, the ultimate strength is growing much slower.

Dilatancy.

Since cracks occupy volume, their formation is accompanied with a decrease in the average matter density. This nonlinear inelastic volume change which accompanies inelastic deformation in brittle materials is commonly referred to as dilatancy or bulking. The basic

observation and defining property of dilatancy is that under increasing deviator stress, many rocks exhibit an increase in volume relative to elastic change, and if stress increases sufficiently, there can be an actual volume increase (Brace et al. 1966). A second characteristic of material that is destroyed by microcracks is hysteresis in physical properties between loading and unloading. This is illustrated in Figure 3 for the compression and unloading under one-dimensional stress conditions. The loading curves consist of three parts. In the initial phase, the microcracks which exist in the incident material and are oriented orthogonally to the applied load obviously are closed elastically. Region 2 is the linear elastic region, from which the rock can be unloaded with no hysteresis. The beginning of region 3 marks the onset of inelastic behavior. Typically this occurs between one-third and two-thirds of the failure stress. The dilatancy and volumetric hysteresis are manifested mostly in the lateral strains, while the axial strain is nearly elastic and almost completely recoverable. The lateral dilatantional strains are attributed to cracks which grow predominantly in the direction of maximum compression. Unloading from region 3 yields a permanent residual volume increment.

For rocks, the magnitude of the dilatancy ranges from 0.2 to 2.0 times the elastic volume changes that would have occurred were the rock simply elastic; the maximum porosity below the failure stress reaches 2% as a result of the dilatancy effect. For deformation up to complete fracture, Grouch, 1970, found the inelastic volume increase between 2% and 5% for quartzite over the whole range past the peak of compressive load. Below the brittle-elastic transition, the magnitude of dilatancy is not markedly affected by pressure. Christensen et al., 1972, have found that the phenomenon of dilatancy under dynamic loading was not significantly different from static conditions. Beyond the point of peak load, the failure becomes unstable. The unloaded density of the material depends on the packing of the granulated debris, assuming the grains themselves have not experienced an irreversible density change. For example, if the material is rubbelized to a collection of spheres, the final density will be only 74 percent of the initial density.
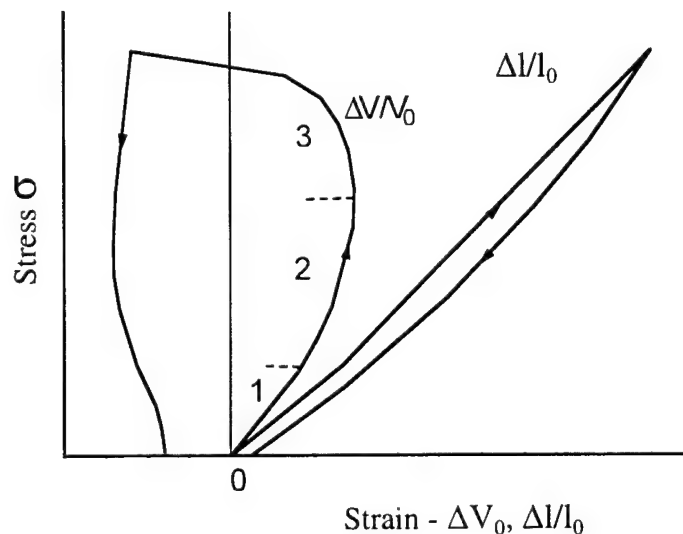
Fig. 3. Quasi-static response of a rock in compression.

There is little hysteresis in longitudinal strain, so it is implied that the volume changes result from the opening of axial cracks. Formation of open axial cracks at a fraction of the maximum stress is also suggested by variations of sound velocity in axial and radial directions: velocity in the axial direction is hardly changed by stress, whereas the sound velocity in a radial direction begins to decrease at about half the failure stress and may drop 10 to 20% (Brace et al. 1966).

Acoustic emission accompanies dilatancy (Kurita and Fuji 1979). When a critical stress level is reached, emissions increase and continue at a high rate until unloading occurs. During unloading and reloading, emissions are substantially reduced until the previous maximum stress is reached, at which point the emission rate rises to its previous high level.

Possible mechanisms of microcracking under compression.

It is known that even when applied stress is wholly compressive, local stress may become tensile at certain points at the crack tip (Griffith 1924, McClintock and Argon 1966) and hence cracks may grow in response to this local tensile stress. Brace and Bombolakis, 1963, observed the growth of cracks in glass and polymer plates under compression. They found that the most severely stressed cracks were inclined at about 30° to the axis of compression. The cracks, when either isolated or placed in an array, grow along a curved path which becomes parallel with the direction of compression, as shown in Figure 4. When this direction is attained, growth stops. The resulting kinked crack consisted of a central crack with sliding surfaces, which is inclined to the direction of compression, and two cracks emanated from its ends, called "wing cracks."
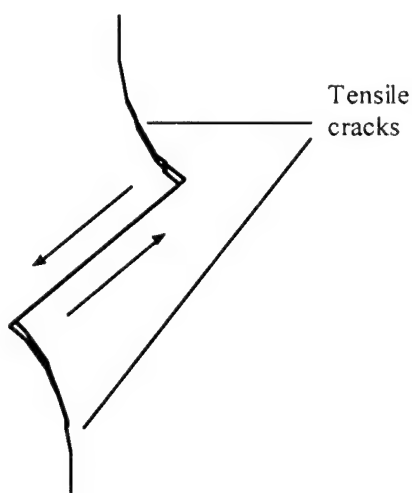
Fig. 4. Wing crack.

More recently a series of similar quantitative experiments was performed by Nemat-Nasser and Horii, 1982, and Horii and Nemat-Nasser, 1985, on thin plates of Columbia Resin CR 39. In a series of experiments they have shown that the relative sliding of the faces of one

8

or even an array of pre-existing cracks leads to the formation of tension cracks which grow in the direction of maximum compression. The model experiments demonstrated that a pre-existing crack close to a free lateral boundary shows no tendency to move toward this free surface under overall uniaxial compression. When great compression had been applied, the load reduction resulted in further crack growth with an immediate tendency to curve toward the free surface. A lateral compression reduces the final crack length, whereas even small lateral tension increases it. In the experiments with specimens containing a number of randomly oriented cracks or rows of inclined coplanar cracks, axial splitting was observed rather than localized shear failure.

When models with various sizes of incident flaws were tested, Horii and Nemat-Nasser, 1985, observed that cracks are nucleated at larger flaws first. The cracks are soon arrested for the specimen with confinement, whereas without confinement they continue to grow while no cracks are nucleated at many smaller flaws. In the presence of confinement, smaller flaws soon become activated, as cracks emanating from larger flaws are arrested because of confining pressure. Then, these smaller flaws interact with each other and nucleate cracks which grow in an unstable manner, leading to final fault.

An interesting observation was done by Chandrasekar and Chaudhri, 1994, in the course of their investigations of the explosive disintegration of Prince Rupert's drops. The internal central region of these drops of rapidly quenched glass is under tensile stress while the surface layer is compressed. High-speed photography indicated that the fast-moving cracks in the tensed central zone slowed down dramatically on entering the surface compression zone of the drops. Microscopical observations of the fragments demonstrated that the fragments from the surface compression zone consist of plates lying almost parallel to one another, as in an onion. The fragments indicate that cracks' surfaces became approximately parallel to the drop's surface as they reached it: the surface compressive stresses constrain the cracks to run parallel to the surface, that means parallel to the compressive stress direction.

Thus, both nature and model experiments illustrate that crack growth in compression is directed preferably along the compression and does not immediately produce a mechanical instability as it does in tension. The stress required to provide a subsequent growth of a crack increases after some crack growth has occurred. Macroscopical faults are form out of a system of cracks.

A sliding crack growth (mode 2, or shear crack) was never observed in the model experiments. Relative sliding of the faces of pre-existing cracks does not result in coplanar crack growth, but rather produces at the tips of the pre-existing crack small tension cracks which deviate at sharp angles from the sliding plane. The model experiments with multiple cracks did not indicate a tendency toward shearing in the plane of cracks either. However, the change of the fracture patterns in rocks with confining pressure suggests that there perhaps is no single mechanism of microcracking.

Modern theories of brittle fracture and dilatancy under compression are mostly based on the development of wing crack models. The wing crack system is really two or three interacting cracks: a shear crack that slides under nonhydrostatic stress to pull open one or two tensile

cracks at the shear crack tips. Friction on the sliding surfaces of the shear crack acts in opposite directions depending on whether shear stress on the sliding surfaces is increasing or decreasing. This provides a hysteresis in the loading-unloading cycle.

However, such wing cracks are very rarely observed in rocks after compression tests. Even with a resolution of 0.01 μm, Tapponier and Brace, 1976, were able to find only a few of them. Sets of grain boundary, low-aspect cavities, as well as suitable oriented interfaces of two different minerals, produced most of the microcracks which were long (a few hundreds microns), and were preferentially oriented with long axes approximately parallel to the axis of maximum compressive stress. On the other hand, it seems reasonable that localized sliding would take place along a plane of high shear, especially if weak areas such as sets of grain boundary cavities or soft inclusions occur at these orientations, and in this way the wing crack model still presents a reasonable idealization. A sliding element of this kind may have frictional resistance, or cohesive shear resistance, or both.

The wing crack model of compression-induced microcrack growth and dilatancy was developed by Holcomb, 1978, Stevens and Holcomb, 1980, Nemat-Nasser and Horii, 1982, Moss and Gupta, 1982, Horii and Nemat-Nasser, 1985, and Nemat-Nasser and Obata, 1988. Within the framework of linear fracture mechanics, Nemat-Nasser and Horii, 1982, analyzed the out-of-plane extension of pre-existing straight crack, induced by overall far-field compression, and quantified various parameters which characterize the growth process. For this, the stress intensity factors at the tip of the kinked extension were obtained, and the kink angle and the corresponding kink length were calculated. For a wide range of pre-existing crack orientations, it was shown that the out-of-plane crack extension initiates at an angle close to 70° from the direction of the pre-existing crack. It was shown that under 1-D stress conditions, the stress intensity factor, K_I, decreases monotonically and goes to zero as the ratio of the kink length to the incipient crack length, l/c, increases. Thus, to increase the kink length, the axial compression must be increased, and therefore the crack growth process is stable. For biaxial loading with lateral compression the K_I value becomes zero at some kink length. This implies that the crack extension is stable and the kink stops at some finite length. On the other hand, when even small lateral overall tension is applied normal to the compressive force, the value of K_I first decreases until a critical kink length is attained, and then begins to increase as l/c increases. This implies that the compressive axial force required to attain the corresponding kink length must first be increased with increasing l/c until the critical l/c is reached, and then it must be decreased with further kink extension. Thus the kink growth under compression with a lateral tension is first stable and then becomes unstable.

The results explain the axial splitting of brittle bodies under compression, although it is evident that interaction between microcracks, which can lead to unstable growth of tension cracks, must dominate the intermediate stages of the failure process of rocks. At certain stages of crack growth the interaction effects become so dominant that only certain cracks continue to grow in an unstable fashion while others are arrested or even closed. It is important also that even when the incident flaws are randomly distributed, their preferential activation, and the nucleation and growth of tension cracks at preferential flaws, render the overall response of the solid highly anisotropic.

In order to estimate contributions of interactions of growing cracks, Horii and Nemat-Nasser, 1985, analyzed rows of oriented flaws. The strength-pressure curve calculated from the model consists of an initial nonlinear part and relatively linear part. In the first part, flaws of maximum size are active. In the second (transition) part the size of active flaws decreases with increasing lateral pressure, and for the last part, which corresponds to the linear segment of the strength-pressure curve, flaws of minimum size are active. The expected overall fault plane angle is rather small for small confining pressure, but it increases sharply and stays around 30° at high pressures.

The dilatancy effect produced by wing cracks was calculated by Holcomb, 1978, Stevens and Holcomb, 1980, Moss and Gupta, 1982, Nemat-Nasser and Obata, 1988. The wing crack models provide excellent qualitative agreement with experimental observations of dilatancy and reasonable quantitative agreement. It is also found that including sliding friction gives larger hysteresis than observed, so the friction coeffecient at unloading must approach zero during unloading (Moss and Gupta 1982).

Continuum failure.

The mechanistic models of flaw nucleation and growth are helpful in understanding mechanisms, but they are too complicated to be used in practical calculations. However, a more integrated constitutive relation with a limited number of the material parameters is needed.

Constitutive modeling of triaxial failure of rocks has been reviewed by Franklin, 1970. In general, theoretical criteria, such as that of Griffith, often give an inadequate fit to the data. Brace et al., 1966, mentioned that the simple process described by Griffith's theory (in which failure results from growth of the critically oriented, most lightly stressed crack) does not correspond to experimental observations: in rocks, crack growth begins at stresses much below the failure stress. Because of that, empirical criteria are developed to meet the practical requirements of accurate strength prediction and simplicity of use. Usually not one, but several empirical criteria can be constructed to fit fracture data. Since different failure mechanisms may operate depending on the region of stress space, different strength criteria should be used at different levels of stress. Some examples of fracture criteria and constitutive models are considered below.

In the dilatancy region, the damage accumulation occurs which determines the subsequent behavior. Costin, 1983, has developed a continuum model for deformation and failure of brittle rock which is based on a simplified mechanics of tensile microcracks. It was assumed that an ensemble of microcracks contained in the body behaves in a manner similar to an individual crack. According to the model, there exists a surface in stress space that defines the onset of damage. The surface is determined by the fracture toughness, K_{IC}, average size of microcracks, a_i, microcracks orientation factor, minimal tensile stress influence distance (of the order of grain size), which is a material parameter, and some nominal threshold stress which is a material parameter also. When the stress state is below the damage surface, no stress-induced crack

growth can take place. For stress states on the damaged surface, crack growth accompanies any increase in loading, and, since the damage surface is controlled by the crack size, it expands.

Figure 5 shows a plot of the damage surfaces in pressure-deviatoric stress coordinates for the i-direction. The initial damage surface in this diagram is a straight line with intercept $S_i^0(a_{i0})$, where a_{i0} is initial crack size. Subsequent surfaces are also straight lines with intercepts $S_i^0(a_i)$. On unloading from a damaged state, the crack size does not change, resulting in a memory of the previous maximum deviatoric stress state.
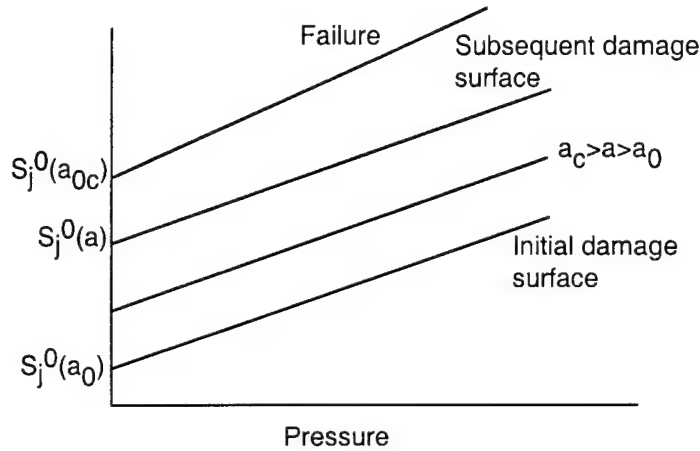
Fig. 5. Initial and subsequent damage surfaces according to the Costin's model.

According to the model, failure occurs when the crack size reaches a critical value a_c, and the failure surface in the pressure-deviatoric stress coordinates should be parallel to the initial damage surface. However, experimental data show a steeper slope of the failure surface than that of the initial damage surface. This is a result of changing mean orientation of active cracks during damage development which the model does not account for. Instead of this, the critical damage size is assumed to be a linear function of pressure to agree with the experimental data.

The model has been incorporated into a constitutive equation which is essentially elastic but accounts for material behavior due to microcrack growth through the inclusion of an internal state variable, $D_i=(a_i-a_0)/(a_c-a_0)$, which is a measure of the crack state. With this constitutive equation, dilatancy in compression is reasonably well described. However, it does not describe well unloading paths or hysteresis at reloading. The model does not address the post-failure region.

In a similar way, Ashby and Sammis, 1990, constructed failure surfaces in stress space which combine information about brittle failure with data describing onset of plastic yielding. The criterion for crack initiation under axisymmetric loading has been chosen to be linear:

$$\sigma_1 = c_1\sigma_3 + \sigma_0,$$

where c_1 and σ_0 are material properties which are determined by the coefficient of friction, crack size, and by the fracture toughness of the material; σ_1 is the axial stress and $\sigma_2=\sigma_3$ the radial stress. Once initiated, the cracks grow longer. During growth, the stress intensity K_I at the tip

12

of each crack is equal to, or exceeds, the fracture toughness K_{Ic} of the material. Based on a simplified model of microcracks, the stress intensity at the tip of the crack has been described as a function of the crack length, coefficient of friction, and center-to-center spacing of cracks. The damage parameter is

$$D = \pi(a-a_0+\alpha a)^2 N_A,$$

where α is a geometric constant and N_A is a number of cracks per unit area. The damage is treated as a state variable. Within the assumption of equal initial crack size, the surfaces of constant damage in stress space are linear. The surface corresponding to final macroscopic fracture is also approximated by a linear relationship

$$\sigma_1 = c_2\sigma_3 + \sigma_c,$$

where σ_c is the simple compressive strength.

As the confining pressure is increased, brittle fracture is made increasingly difficult. A critical pressure may be reached at which true plasticity replaces crack extension. The yield surface is described by Von Miezes criterion

$$\sigma_y^2 = 0.5 \cdot [(\sigma_1-\sigma_2)^2+(\sigma_2-\sigma_3)^2+(\sigma_3-\sigma_1)^2] ,$$

where the yield strength, σ_y, is derived from hardness, H, data since $\sigma_y = H/3$. As a result, the failure surface takes a shape shown in Fig. 6. The model has been fitted to data for number of rocks.
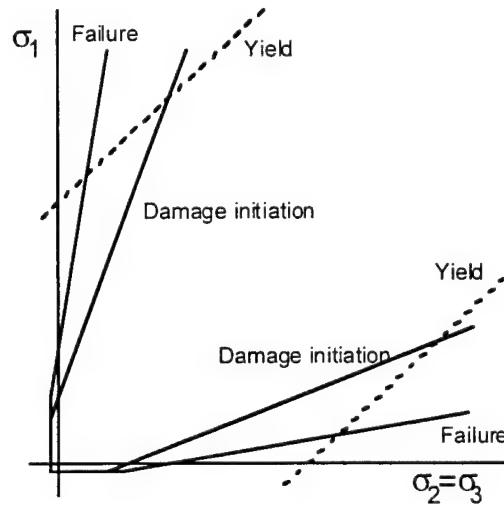
Fig. 6. Failure and yield surface according to Ashby and Sammis, 1990.

3. DYNAMIC TEST TECHNIQUES

Experiments with shock waves.

Shock loading a sample with the impact of projectile, the detonation of high explosive, or the rapid deposition of radiant energy produces an inertial response with the stress- or particle velocity-time histories which depend upon the compressional properties of the sample (Zel'dovich and Raizer 1967). A shock wave occurs as a rapid change in stress, density, and particle velocity in the flow. The conservation equations for mass, momentum, and energy which govern the flow field for steady shock waves propagating in the x direction are:

Conservation of mass $\qquad\qquad \rho_0 U_s = \rho(U_s - u_p)$

Conservation of momentum $\qquad\quad \sigma_x = \sigma_{xo} + \rho_o U_s u_p$

Conservation of energy $\quad \rho_o(E - E_o) = -\frac{1}{2}(\sigma_x - \sigma_{xo})\left(\frac{\rho_o}{\rho} - 1\right)$

where U_s is the shock velocity, u_p is particle velocity, ρ_0 and ρ are the initial and current values of the density, σ_{x0} and σ_x are the total mechanical stress in the direction of propagation before and after the shock, and E_0 and E are the internal energy before and after the shock. Collectively, these equations are known as the Rankine-Hugoniot jump conditions. The Rankine-Hugoniot curve, also known as the Hugoniot or shock adiabat, is the locus of end states achieved through steady shock-wave transitions. Usually the initial state of the condensed material is at rest and with zero stress, but Hugoniot curves can also be defined for other initial conditions.

Under moderate compression (less than 1 Mbar), Hugoniots of condensed media are usually described by linear relationships of the form $U_s = c_0 + s \cdot u_p$, where the first term, c_0, is close to the sound velocity corresponding to the initial equilibrium bulk compressibility of the medium and s is a material constant with values usually in the range of 1.0 to 2.

In plane shock waves the boundary conditions are uniaxial strain. Figure 7 shows the stress-strain diagram for a solid body under one-dimensional compression during both loading and unloading. In the elastic region, the longitudinal module of the material is

$$\frac{d\sigma_x}{d\varepsilon_x} = -V\frac{d\sigma_x}{dV} = K + \frac{4}{3}G.$$

This uniaxial strain modulus is larger than the bulk stiffness:

$$-V\frac{dp}{dV} = K$$

which approximately represents the material stiffness during yielding. The yield condition under uniaxial strain conditions is satisfied when

14

$$|\sigma_x - p| = |S_x| = \frac{2}{3}Y.$$

Thus the longitudinal stress in an elastic-plastic body deviates from the hydrostatic curve $p(V)$ by not more than $2Y/3$. The longitudinal stiffness during plastic deformation is approximately the bulk stiffness. Combining the yield condition with the longitudinal stiffness relation, we obtain the longitudinal stress at initial yield:

$$\sigma_x = -Y\left(\frac{K}{2G} + \frac{2}{3}\right).$$

Here K and G are the bulk and shear moduli. This initial yield value for the longitudinal stress under shock wave loading is called the Hugoniot Elastic Limit (HEL). During unloading under planar wave propagation conditions, the stress σ_x initially decreases elastically. Reverse yielding occurs after the deviator stress S_x passes through zero and increases to yielding again. The decrease in the stress σ_x to reach reverse yielding is approximately twice the HEL.

With this background on the yield process in ideal plasticity, let us now examine the wave processes illustrated in Figure 7. The stress history at the impact surface consists of a jump, a plateau, and then a gradual decrease in stress corresponding with the rarefaction proceeding from the rear of the impact plate. After the wave has passed through some of the elastic-plastic target material, considerable structure has developed. As a result of different longitudinal compressibilities at stresses below the HEL and above it, the shock wave becomes unstable and is split into an elastic precursor wave, which propagates with the longitudinal elastic wave speed, and a plastic shock wave with a lower propagation velocity. The peak stress behind the elastic precursor front is

$$\sigma_{HEL} = (1\text{-}\nu)Y/(1\text{-}2\nu) = (2/3)Y_c/(1\text{-}c_b{}^2/c_l{}^2) = (1/2)(c_l/c_s)^2,$$

where ν is the Poisson's ratio, and c_l, c_s, c_b are longitudinal, shear, and bulk sound velocities, respectively. Thus the wave front shows first the arrival of an elastic precursor with an amplitude corresponding to the HEL. The wave velocity of the precursor corresponds to the elastic wave velocity which in this uniaxial stress case is the velocity c_l of longitudinal elastic waves:

$$c_l = \sqrt{\frac{K + \frac{4}{3}G}{\rho}}.$$

The remainder of the compressional wave arrives with the shock velocity $U_s \geq c_b$, where c_b is the "bulk" sound velocity:

$$c_b = \sqrt{\frac{K}{\rho}}.$$

15
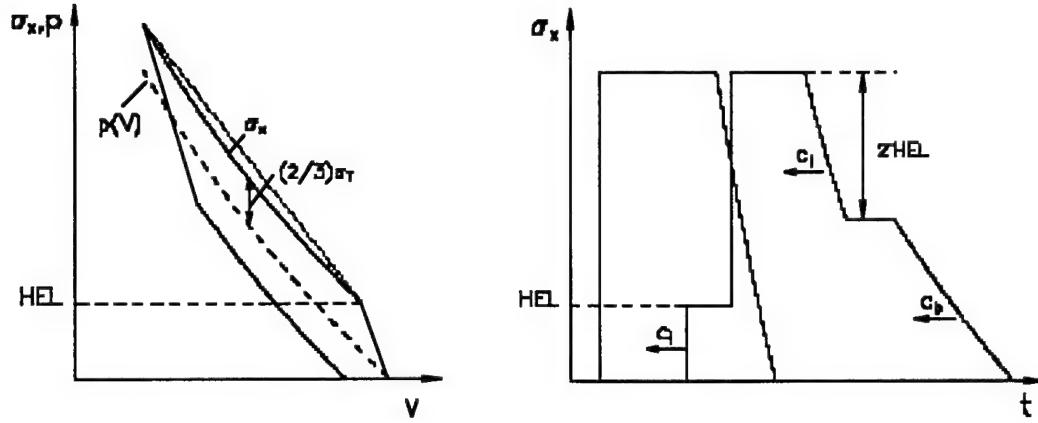
Fig. 7. The stress-strain path of 1-D strain elastic-perfectly plastic deformation and corresponding stress histories at different distances in a shocked body.

The plastic shock front velocity U_s corresponds with the slope of the Rayleigh line connecting points at HEL and at the peak stress state

$$\sigma_x - \sigma_{HEL} = \rho_0^2 U_s^2 (V_{HEL} - V),$$

where V is the specific volume of compressed matter and V_{HEL} is the specific volume at the Hugoniot elastic limit. Following the plateau on the second wave history, the stress decreases by twice the HEL, then reverse yielding occurs. Following this reverse yielding the remainder of the wave travels at a slower range of velocities corresponding with the bulk sound speed, which is a function of the stress level.

It must be emphasized that real materials rarely exhibit the simple elastic-perfectly plastic response. In many instances, strain hardening occurs, whereby the yield stress increases under shock. In the case of brittle behavior, material softening may be expected. Finally, under shock wave conditions all materials demonstrate more or less pronounced rate-dependent behavior. The Hugoniots of strain-hardening and strain-softening materials are shown schematically in Figure 8. For an elastic-perfectly plastic solid the plastic shock speed $U_s \cong c_b$; for an elastic-strain hardening plastic solid the plastic shock wave speed is always greater than the bulk sound speed. In the case of elastic-strain softening solid the plastic shock wave speed can be less than c_b. It can be shown (Kanel et al. 1996) that, when strain hardening of the material is described by a formula

$$Y = Y_0 + q\gamma^n,$$

where γ is the plastic strain, Y_0, n are parameters of the material and $n \leq 0.5$, a ramping growth of the stress or particle velocity appears immediately behind the elastic precursor front. Another reason of the ramping can be a stress relaxation behind the elastic front.

Viscous stress relaxation also affects the rise time of a second inelastic compression wave. The rise time of a steady compression wave is determined by both material relaxation properties and the amplitude of the wave. The amplitude dependence of the rise time has been shown to exhibit a more or less common trend over a range of ductile and brittle materials (Swegle and Grady 1985).

16
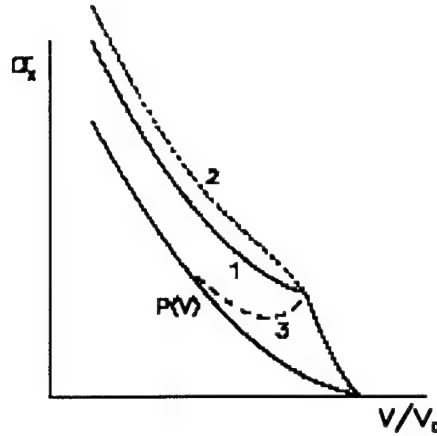
Fig. 8. Idealized Hugoniots for an elastic-perfectly plastic solid (curve 1), an elastic-strain hardening plastic solid (curve 2), and an elastic-strain softening or elastic-isotropic solid (curve 3).

In the first studies, the relationship between the measured Hugoniot $\sigma_x(V)$ and an "isotropic Hugoniot" $p(V)$, which was calculated based on results of hydrostatic measurements, was used to evaluate the yield strength of ceramics in shock-compressed state (Ahrens et al. 1968, Graham and Brooks 1971, Gust and Royce 1971). It was thought that the Hugoniot $\sigma_x(V)$ should be shifted up relative to the "isotropic Hugoniot" $p(V)$, and measurements of this stress offset $\sigma_x - p$ should indicate whether the shock-compressed material keeps its yield strength, which implies elastic-plastic behavior, or whether the yield strength drops to zero, which implies elastic-isotropic response. However, scatter in the shock-wave data and possible systematic error in the hydrostatic measurements did not always permit definitive conclusions. Thus, B$_4$C and Si$_3$N$_4$ appear to have values of c_0 in a linear relationship between shock velocity and particle velocity, $U_s = c_0 + s \cdot u_p$, significantly less than the bulk sound speed c_b, perhaps indicating significant loss of strength (Grady 1998). However, aluminum retains strength to high compression (Ahrens, 1968).

Modern shock-wave experiments with brittle materials include measurements of the Hugoniot over a wide stress range, Hugoniot elastic limit (HEL), the shock front rise time, the stressed state immediately after the shock compression, unloading path from the shock-compressed state, tensile strength after shock compression below and above the elastic limit, and post-test examination of recovered samples. Figure 9 shows a typical particle velocity history measured by Kipp and Grady, 1990, for SiC and B$_4$C ceramics using a VISAR laser Doppler velocimeter (Barker and Hollenbach 1972) through an LiF window.

17
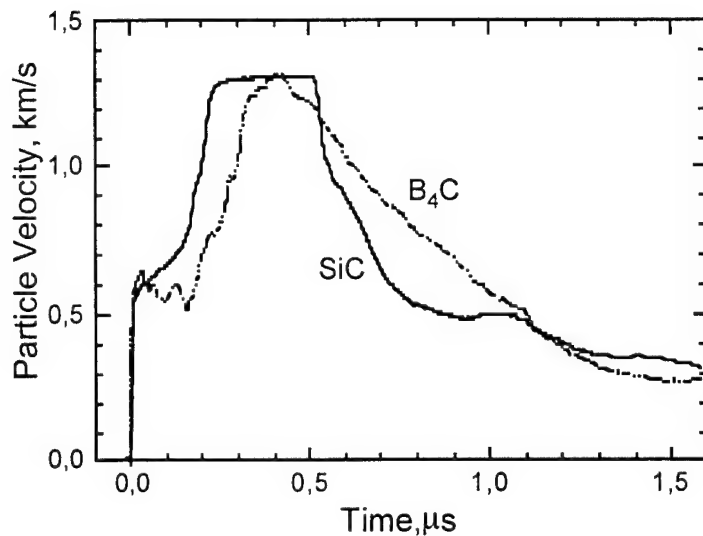
Fig. 9. Particle velocity profiles for SiC and B₄C ceramics measured at the interface with an LiF window (Kipp and Grady 1990).

Post-yield strength of silicone carbide, determined by comparison of Hugoniot uniaxial strain and calculated hydrodynamic response, reveals neutral or increasing strength with subsequent deformation beyond the initial dynamic yield (Kipp and Grady 1990). Boron carbide, in contrast, indicates a dramatic loss in strength. Correspondingly, post-yield characteristics of the precursor waves are dramatically different for these two materials. For silicon carbide, positive slope of the wave demonstrates strain hardening. The stress drop after the HEL in boron carbide, in contrast, indicates post-yield softening.

Another reason for the ramping behind the precursor front in SiC can be a stress relaxation. The stress relaxation determines also the rise time of the second inelastic compression wave and the ramped stress pulse top. The additional disturbance in the structure of the second wave is a result of precursor and secondary wave interactions at the target/window interface. The chaotic particle velocity oscillations in boron carbide are apparently caused by a heterogeneous failure or faulting mechanism during compressive loading. The unloading wave for boron carbide is much more dispersive than for SiC, and this shows that only the very start of the release is indicative of purely elastic behavior. The inelastic strain starts almost immediately behind the rarefaction wave front in B₄C.

Measurements of stressed state of shock-compressed matter.

The stressed states of shock-compressed solids can be measured directly without computations of hydrostat. The scheme of measurements is shown in Figure 10. The specimen is assembled of several plates in such configuration to have thin plane gaps which are oriented

perpendicular and parallel to the direction of shock compression. The gaps are filled with soft polymer films which serve as insulators for pressure gauges placed in the gaps. Behind a shock front, the pressure in the gap which is perpendicular to the direction of compression becomes equal to the axial stress, σ_x, in the specimen, while the pressure in the transverse gap is equal to the tangential stress σ_y. With the pressure gauges the stress histories as a function of time in both gaps, $\sigma_x(t)$ and $\sigma_y(t)$, are recorded. Figure 11 shows an example of longitudinal and lateral stress histories measured with the manganin piezoresistive gauges at a shock compression of glass sample.

Sample plates

Base plate
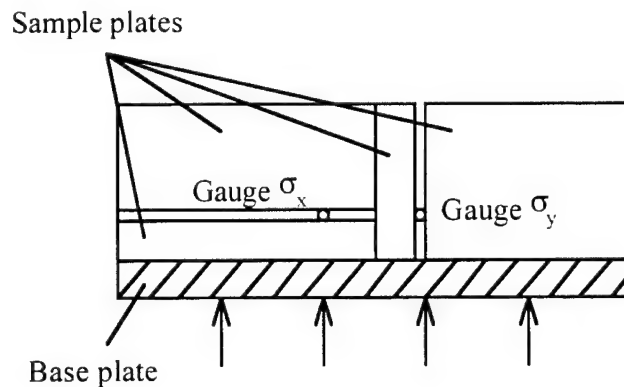
Fig. 10. Schematic view of a shock-wave experiment with simultaneous measuring of the longitudinal (σ_x) and lateral (σ_y) normal stress components.
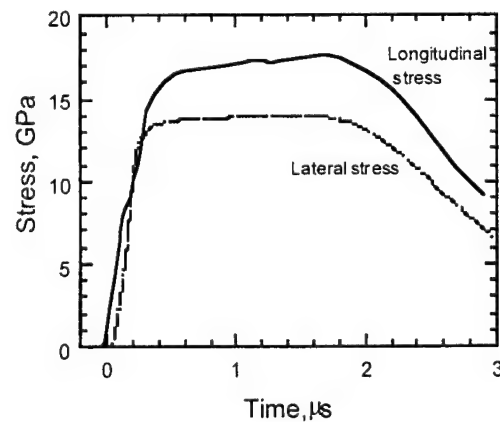
Fig. 11. Longitudinal and lateral stress histories at shock compression of a glass sample. Measurements with the manganin piezoresistive gauges.

The direct measurements of stressed states in shock-compressed solids are still accompanied by several sources of uncertainties. The stress equilibration on the σ_y gauge takes much more time than on the σ_x gauge, so measurements of lateral stress are possible only at later times behind the compression front. Feng et al., 1997, performed two-dimensional computer simulations of the shock-wave processes in the assembly shown in Figure 10. The

results show that the mechanical states within and near the lateral gauge deviate significantly from uniaxial strain due to perturbations caused by the gap emplacement. However, the established equilibrium gauge response is a good measure of the far-field, lateral stress in the shocked sample. Besides this, deformation of the piezoresistive gauge may also influence the signal.

Evaluation of a complete stress-strain trajectory of shock compression and unloading of the material is another way to extract insight from shock tests. In particular, this stress-strain trajectory (Kipp and Grady 1990) for B_4C ceramic shows unambiguous evidence of dilatancy when the compressive stress approaches zero at unloading, while the SiC ceramic demonstrates a typical "elastic-plastic" yielding behavior.

Experiments with plane shock waves provide an ability to study mechanical properties of materials under high pressure and extreme high strain rate. However, the typical strain values are small in the plane shock waves, and increase in the strain is usually connected with a pressure growth. It would be desirable to expand the possibilities of plane-wave experiments to larger deformations. New prospects in this regard can be reached if the impact loading were cylindrical or spherical symmetry. An additional transverse deformation which is proportional to the radius increment will increase the total strain in this case. Behavior of alumina submitted to a divergent spherical stress wave was studied by Tranchet and Collombet, 1995. In experiments performed by Kanel et al., 1998, the cylindrical shock loading of alumina tubes was realized with detonation of an explosive charge. Lagrangian 1-D computer code for simulations of the shock-wave processes with axial symmetry has been used to interpret the VISAR measurements of the velocity profiles. The strain range available for analysis has been extended by a factor of two or three due to the divergent character of flow.

Spall strength.

When a compression pulse is reflected from the body free surface, interaction of two rarefaction waves produces tensile stresses inside the body which may cause a tensile fracture. This kind of dynamic fracture is called "spall fracture" or "spallation."

Two ways can be utilized to find the fracture stress under spall conditions, or so-called "spall strength." The first is based on examination of recovered samples after a series of impact loading at varied peak stress. By this way a stress threshold corresponding to appearance of a first damage is determined. The second and most common way is based on measurements of the velocity history of the sample free surface. Fracture of material allows the tensile stress to decrease rapidly to zero. As a result, a compression wave appears in stretched material adjacent to the spall plane. This wave propagates to the free rear surface and forms a so-called spall pulse in the free surface velocity profile, $u_{fs}(t)$. Subsequent reverberations of the spall pulse between the free surface and spall plane are accompanied by damped oscillations of u_{fs}. The period of velocity oscillation is a measure of the thickness of the spall plate. The velocity pullback Δu_{fs} is a measure of incipient fracture strength, σ^*, of the material:

$$\sigma^* = \frac{1}{2}\rho_o c \cdot (\Delta u_{fs} + \delta),$$

where δ is a correction for the profile distortion due to the elastic-plastic properties of the material (Kanel et al. 1996), and c is the sound velocity. If the interaction of incident and reflected rarefaction waves occurs within the elastic deformation region, then $\delta = 0$, $c = c_l$.

Tensile stresses are created inside of a body due not only to reflection of compression pulse from the free surface but also due to reflection from an interface with a softer material. Some measurements of spall strength are based on the pressure profiles on this boundary. Replacement of the free surface by a soft barrier leads to an increase in the distance between the spall plane and the plane at which measurements are made. As a result, the possible distortion of wave profile also increases if the interaction of incident and reflected rarefaction waves occurs in the plastic deformation region. Additional sources of error in this case are in the equations of state used for the sample and barrier materials and in precision of pressure gauges, which is limited by the accuracy of their calibration.

Figure 12 shows a free surface velocity profile of a sample of a ceramic consisting of titanium carbide particles bonded by nickel (Kanel and Pityulin 1984). The mass fraction of titanium carbide in the composite was 80%. The free surface velocity records do not show a well-pronounced elastic precursor in the wave profile of this ceramic. This is due to wave dispersion caused by multiple reflections of the stress waves between constituents with different dynamic impedances. The spall strength is 0.4 to 0.55 GPa, and it decreases with increasing peak stress. Since the spall strength of nickel is 3 to 4 times higher than the values measured for the titanium carbide-nickel ceramic, the results confirm that fracture nucleates in the brittle titanium carbide phase.

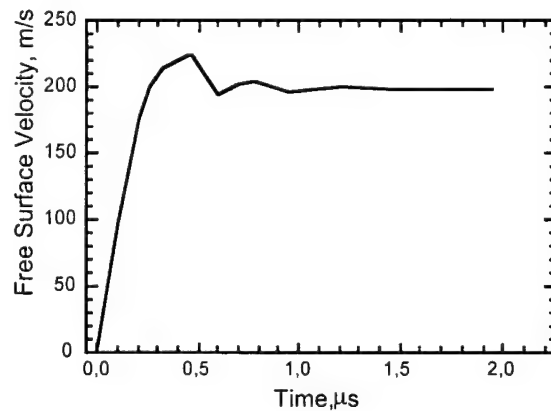Fig. 12. The free surface velocity history of TiC+Ni cermet sample 10 mm thick impacted by aluminum flyer plate 2 mm in thickness at 450 m/s impact velocity.

Ceramics and rocks exhibit a dynamic tensile strength in a range of 50 to 500 MPa. Nevertheless, the dynamic fracture strength of rocks can exceed the static tensile strength by as much as one order of magnitude. In the reviews of fracture mechanics under high-rate loading,

Grady, 1985, 1988, discussed a correlation between the spall strength of rocks and their fracture toughness. Accounting for the dynamic stress intensity factor, which is a function of the crack size and time, the strain-rate dependent fracture stress is determined as

$$\sigma_c = \left(\frac{9\pi E K_{1c}^2}{16 N^2 c_s}\right)^{1/3} \dot{\varepsilon}_0^{1/3}$$

where N is a geometrical coefficient equal to 1.12 for the penny-shaped crack, and c_s is the shear wave velocity. This equation corresponds to the stress level required to initiate fracture on an isolated, normally-oriented circular crack which is sufficiently large relative to the load conditions specified by the strain rate $\dot{\varepsilon}_0$. In a body with a distribution of flaws under similar loading conditions, fracture initiation occurs on the flaws with a characteristic size of the order $a \approx (c_s K_{1c}/E\dot{\varepsilon}_0)^{2/3}$. Comparison of dynamic spall data for rock with the criterion shows a reasonable correlation.

The spall strength measurements may diagnose the degree of damage of the material in the incident compression wave. Localized microfractures in brittle ceramics and rocks can appear at inhomogeneities during the compression phase even when the deformation of the material as a whole is elastic. The degree of fracture increases with increasing load intensity, and the damage that occurs under compression decreases the capacity of the brittle material to resist the tensile stresses that follow the initial compression phase.

Rod impact experiments.

The rod impact experiment is a useful technique for measuring the yield strength of ductile and brittle materials at strain rates in the range 10^2-10^4 s^{-1} under conditions of the uniaxial stress state. This test can also be used to quantify dilatant behavior in brittle materials.

Figure 13 shows schemes of the rod impact experiments. Different versions are used. In earlier work by Janach, 1976, rock cylinders were made to impact on a stationary steel bar, which was instrumented with strain gauges to record the stress pulse during failure of the specimen. The advantage of the symmetrical impact technique, with one moving and one stationary rod of the same material, is that the processes in both specimens are identical. Therefore all gauges can be installed on the stationary specimen without any loss of information. This experimental arrangement is optimal also for analysis and computer simulations. To create the load pulse with the rise time close to that for a steady stress pulse in a rod, Chhabildas et al., 1998, used impactor plates made of graded-density materials. An electromagnetic technique or VISAR laser Doppler velocimeter and manganin pressure gauges are usually used to record the particle velocity and the stress histories of the load pulse in the impacted sample. Besides this, the fracture pattern and the sample expansion are recorded with a high-speed photography technique. Glenn and Janach, 1977, used an electromagnetic technique to record the temporal variation of the radial particle velocity component on the surface of granite cylinders.
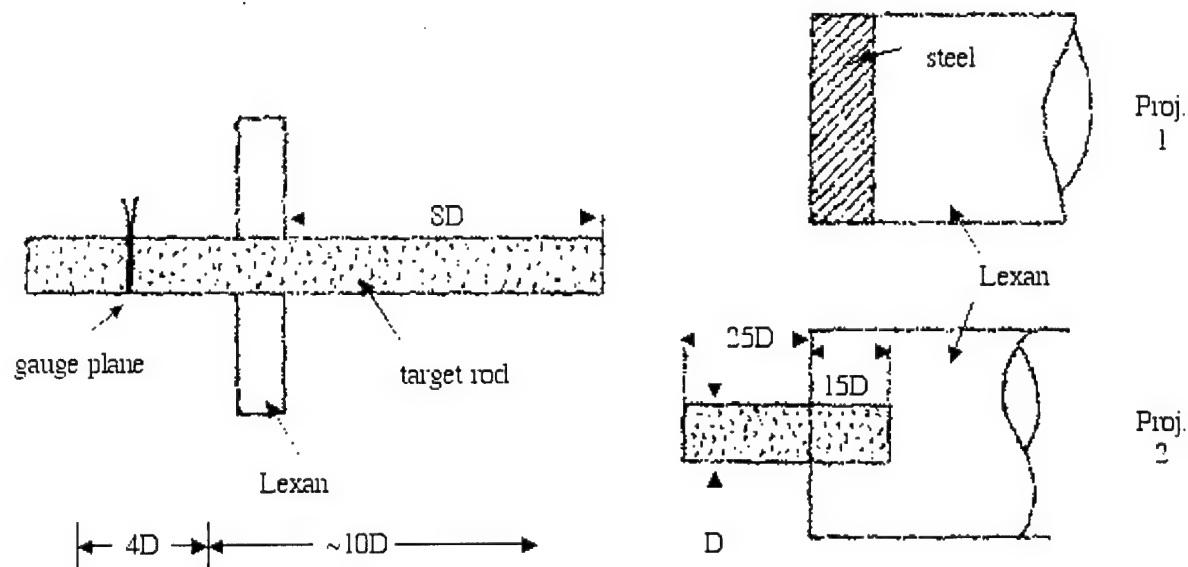
Fig. 13. Schemes of the rod impact experiments.

After a low-velocity impact, an elastic wave propagates down the bar. Near the impact surface (less than about two rod diameters) the stress state is 1-D strain, while at larger distances the 1-D stress state is formed. Under impact conditions, the formation of a uniaxial stress wave occurs through multiple wave reverberations in the radial direction. During these radial pulsations, a tension can be created for a short time in the vicinity of the rod axis (Simha et al. 1999). As a result of dispersion in the bar due to two-dimensional effects, the compression wave forms immediately at the impact surface. It has a rise time corresponding to a few wave reverberation periods across the cylinder radius. The load duration in each cross section of the sample rod is controlled by the wave reflections from free ends of the impactor and the sample rod, which unload the stressed state. The length of rods has to be chosen so that reflections from the free ends do not arrive during the time of interest, and it has to be large enough to build up the 1-D stress wave.

For ductile materials, one uses an impact velocity that causes plastic flow on the impact face of the bar. The amplitude of the stress wave is the largest compressive elastic stress that can be sustained in the bar material, σ_c. Near the impact surface, where the stress state is 1-D strain, $\sigma_c = \sigma_{HEL}$. At larger distances $\sigma_c \rightarrow Y_0$, the yield stress for 1-D stress deformation. For the strain-hardening materials the plastic wave is also formed which propagates much slower than the elastic wave. So the stress level $\geq Y_0$ is supported until the unloading wave from a free end of the rod assembly will arrive. The behavior of brittle materials is similar to that of ductile materials when the impact stress does not exceed some threshold value. When the impact velocity is increased in order to generate higher impact stress, the axial stress begins to unload immediately with a gradual decrease as a result of the failure process in the specimen. The failure proceeds more rapidly as the impact stress is increased. As a result, a short load pulse is formed and propagates down the bar whose amplitude corresponds to the failure threshold

23

under 1-D stress conditions. However, Simha et al., 1999, have pointed out that under some conditions in brittle bars the propagative stress is reduced by tensile failure during the early time reverberation.

Split Hopkinson pressure bar technique.

With the split Hopkinson bar dynamic compression technique, the dynamic stress-strain relation is obtained by sandwiching a small sample between two elastic bars of common cross-sectional area and elasticity, called the incident bar and the transmission bar, respectively. An elastic stress pulse is introduced into the incident bar by impact and is transmitted through the sample into the transmission bar. The impedance of the specimen should be lower than that of the bar so ceramic samples of a small diameter are tested to reach the failure threshold. The stress pulse in both bars are measured so the stress history in the sample corresponds to the measured transmitted pulse, and the strain of the sample is calculated from the pulse reflecting off the sample back into the incident bar. In such an experiment, the stress in the sample fully builds up to the maximum after a number of reflections between the two adjacent steel bars. The loading time is proportional to the specimen length and the number of reflections. As soon as the stress level is high enough, failure will start while loading is still in progress. For brittle materials, it is important to ramp the input pulse so that the failure does not occur before the specimen reaches stress equilibrium (Forrestal 1999.)

4. DYNAMIC STRENGTH PROPERTIES OF SINGLE CRYSTALS AND GLASSES

Quartz.

According to Wackerle, 1962, the Hugoniot elastic limit for quartz single crystals is between 5.5-8.5 GPa for shocks in the x-axis direction and 10-15 GPa along the z-axis. Above the HEL a catastrophic loss of shear strength was observed, so the shock-compressed states are no longer related to the sample orientation. Careful measurements performed by Graham, 1974, have shown a definite offset between the isotropic hydrostatic equation of state and the shock-compression data. Nevertheless, this offset is considerably less than that corresponding to the shear strength of 6 GPa HEL in x-cut quartz. From an analysis of piezoelectric output of shock-compressed quartz it also was concluded that between 4 and 6 GPa the stress at the impact surface relaxed to lower stress values in times of about 10^{-8} s. Photographs of shock-compressed x-cut quartz (Brannon et al. 1984, Schmitt et al. 1986) display a spotty, heterogeneous radiation field that indicates heterogeneous shock deformation. The onset of luminosity between 4 and 6 GPa coincides with dynamic yielding. The emission occurs along discrete lines which lie along the intersections of known fracture planes with the YZ plane. As the stress is increased moderately beyond the HEL, the emission pattern becomes

homogeneous. The emission spectra represent nonthermal radiation combined with gray body radiation and are similar to the photoluminescence from structural defects.

Anan'in et al., 1974, have revealed glass-like interlayers between quartz blocks in recovered single crystals. This lamellae structure indicates a heterogeneous nature of shock deformation of quartz, accompanied by melting. Grady, 1980, has developed a model of localized dissipation of elastic strain energy in low thermal conductivity strong solids which results in an adiabatic shear band. It is supposed that the local dissipation of the elastic shear strain energy leads to local temperature growth which reduces the local flow stress causing the shear strain and the energy release to be localized within narrow bands where the temperature may reach melting.

The direct high-resolution measurements of the shock wave profiles for quartz are complicated by piezoelectric effects and, it seems, by a nonuniformity of the shock-wave process. Figure 14 shows the VISAR free surface velocity profiles measured below the HEL in experiments with large load durations. At 3.5 GPa peak stress the velocity history corresponds to the purely elastic response of the matter. The negative velocity pullback is a result of the wave re-reflection from a copper base plate used in the experiment. Reproducibility of the measurements decreased when the peak stress was increased up to ~5.5 GPa. Chaotic oscillations appeared in the velocity history near the HEL that probably are evidence of localized inelastic deformation or cracking.

Figure 15 shows free surface velocity profiles for x-cut quartz samples for very short load durations (Kanel et al. 1992). The free surface velocity profile corresponding to a shock pulse amplitude of 2.8 GPa replicates the form of the compression pulse inside the sample and does not display any symptoms of spallation. Increasing the pulse amplitude to 4.6 GPa causes spall damage, as evident from the spall pulse in the free surface velocity profile. A further increase in pulse amplitude to 5 GPa modifies the free surface velocity profile dramatically. The unloading part of the pulse is not manifested at the surface, which means that the tensile strength is practically zero in this case. Cracking in the brittle single crystal under compression is a plausible explanation for the diminishing tensile strength near the HEL.
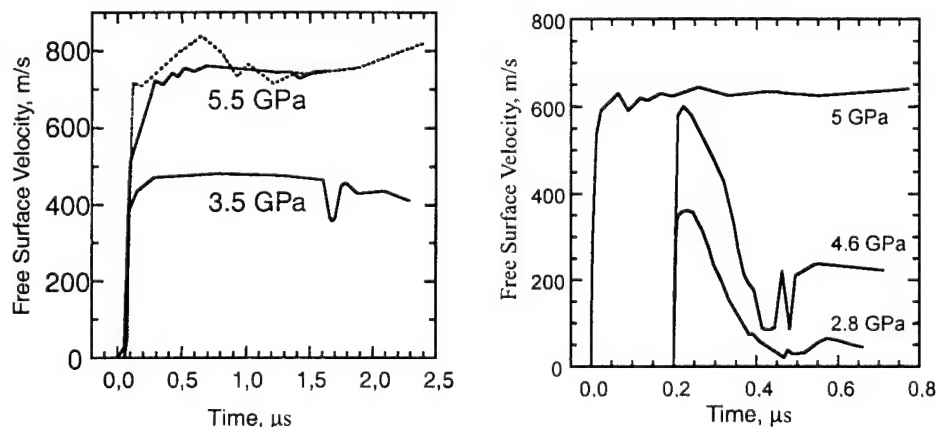

Fig. 14. (Left) The free surface velocity profiles for x-cut quartz samples 4 mm thick.

Fig. 15. (Right) The free surface velocity profiles for the x-cut quartz at different peak stresses generated by aluminum impactor plates 0.2 or 0.4 mm in thickness.

25

Thus, the high homogeneity of sapphire and quartz single crystals allows them to sustain very high tensile stresses. This is because, for such materials, generation of large tensile stresses without any plastic deformation is possible if the compressive stress is below the HEL. In this case, fracture initiates at a structural level near that of the ideal crystal lattice.

Sapphire.

Graham and Brooks, 1971, compared the Hugoniot of sapphire to hydrostatic data. The shock-wave experiments have been performed with sapphire samples of three different crystallographic orientations to the load direction: 0° (crystallographic orientation [0001]), 90° (crystallographic orientation [$\bar{1}2\bar{1}0$]), and 60° (crystallographic orientation [$11\bar{2}3$]). The results are shown in Figure 16. Even though sapphire has trigonal symmetry, the elastic stiffnesses do not vary significantly with orientation: the longitudinal wave speeds in the 0° and 90° orientations differ by only 0.5 per cent. The observed HEL varied from 12 to 21 GPa around an average 8-15 GPa of the mean value for sample thicknesses 6 to 13 mm. Barker and Hollenbach, 1970, detected erratic optical behavior of sapphire at the shock stress of about 15 GPa that was treated as an onset of plastic yielding. Over the elastic range, sapphire exhibits slightly nonlinear longitudinal shock compressibility, which is described as $U_s=11.19+u_p$, (units of km/s) (Barker and Hollenbach 1970) or $U_s=11.17+0.95u_p$ (Mashimo et al. 1987) at the initial density of 3.986 g/cm^3. Above the HEL, all the states of shock-compressed sapphire fall on a common compression curve, independently of the orientation, the sample thickness, and the HEL value. The Hugoniot shows a collapse toward the isotropic compression curve: the stress offset above the HEL is 3.8 to 4.3 GPa, while at the HEL it ranges from 5.5 to 11 GPa. The collapse is confirmed by a direct comparison of the second-wave shock velocity just above the HEL and the bulk sound speed: subsonic waves are observed in this stress region.

Mashimo et al., 1987, in general, have confirmed the Hugoniot data measured by Graham and Brooks. The HEL stresses were determined to be 14.4-17.3 GPa. However, using a different hydrostat than that of Graham and Brooks, they found a stress offset of 6.5-8 GPa above the HEL that does not differ so much from these values at HEL. The data are shown in Fig. 16. The stress histories measured with manganin pressure gauges showed very similar shapes to that of a perfect elastoplastic material.

Wang and Mikkola, 1992, examined the recovered sapphire samples with transmission electron microscopy after shock compression up to 23 GPa. The recovery procedure permitted numerous reflected waves so that fragmentation of the specimens occurred. Within the fragments, a significant number of slip bands in different crystallographic directions suggested that a large amount of plastic deformation has occurred at shock stresses of 12 GPa and more. Changing the crystallographic orientation with respect to the shock wave direction had a significant influence on the substructure developed. Shock loading at 23 GPa with ($10\bar{1}2$) plane perpendicular to the shock wave direction introduced a volume fraction of twins of 0.176 that should provide 9% plastic strain. Unlike quartz, no signs of local melting were observed.

Spall experiments were carried out with ruby (Razorenov et al. 1993) and sapphire (Kanel et al. 1994). Measurements shown in Figure 17 were made at shock wave intensities below the Hugoniot elastic limit. The spall strength of ruby was found to be equal to 8.6 GPa at 15.1 GPa peak shock stress, and 10 GPa at 13.5 GPa peak stress. The spall pulse had a drastically steep front, indicating a very fast damage evolution process. No spallation was observed in the shot with sapphire at much shorter load duration, where the shock intensity was 23 GPa and the peak tensile stress reached 20 GPa. In the other shot at 24 GPa peak shock stress, spallation was observed at a tensile stress of 10.4 GPa. The extraordinarily high spall strength of this material is attributed to lack of flaws and heterogeneities.

Iron-silicate almandine-garnet single crystals were tested by Graham and Ahrens, 1973, who were trying to detect a polymorphous transformation which occurs when static pressure exceeds 19.5±2 GPa. The HEL values achieved by the individual garnet samples occurred over an extended range of stress levels around the average value of 8.1±1.7 GPa for shocks in the [100] direction. The corresponding stress offset between the HEL and the hydrostatic Hugoniot is 2.7±0.7 GPa. Since the final shock-compressed states beyond the elastic deformation region correspond well to the hydrostatic data, it was concluded that, in fact, garnet behaves as a fluid above the HEL.
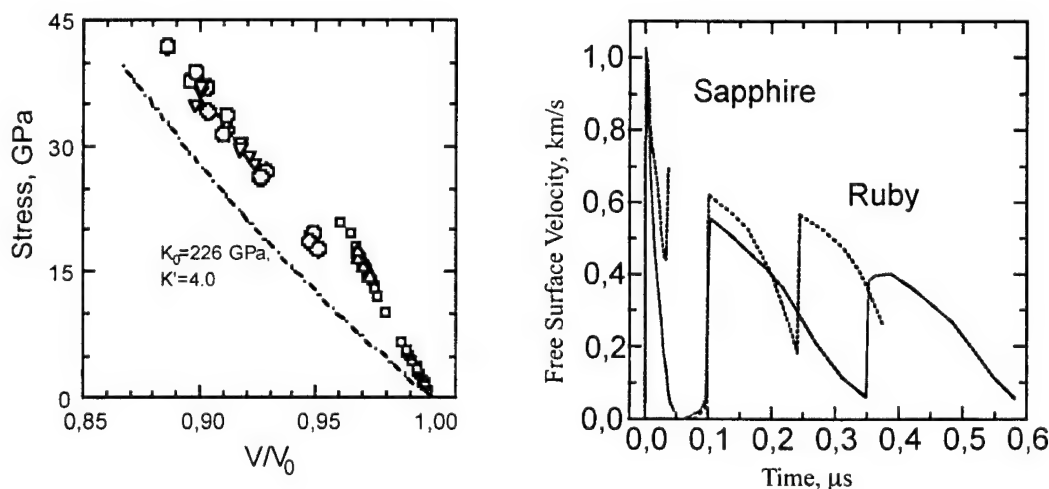
Fig. 16. (Left) Stress-volume relations for sapphire under shock-wave compression. Squares and circles present the experimental data by Graham and Brooks, 1971; triangles present the data by Mashimo et al., 1987. The dot-dashed line shows the isotropic compression curve used by Mashimo et al., 1987.

Fig. 17. (Right) Free surface velocity profiles measured in the spall experiments with ruby (Razorenov et al. 1993) and sapphire (Kanel et al. 1994). The ramped precursor at profiles for ruby is a result of the air shock.

Olivine single crystals of approximate composition $(Mg_{0.9}Fe_{0.1})_2SiO_4$ were tested by Furnish et al., 1986. The measured particle velocity profiles are similar to that for B_4C shown in Fig. 9. The elastic precursor wave with a rise time <10 ns and the peak stress of 6.5 GPa at

shocking along the *a*-axis and 7.8 GPa at shocking along the bisector of the [100] and [013] directions is accompanied with the stress relaxation and small high-frequency excursions. The stress relaxation is much more pronounced at loading in the bisector direction. The shock-compressed state behind the second shock wave corresponds well to a calculated "bulk" isentrope. The release wave gradually decreases the particle velocity and the stress. The release curves in the stress-density coordinates are close to the isentrope, indicating much less shear stress than at the Hugoniot elastic limit.

Thus, hard single crystals show a more or less substantial reduction in shear strength at shock compression beyond their Hugoniot elastic limits. Within the elastic strain range they demonstrate very high dynamic tensile strength as a result of their high homogeneity. Above the HEL they often show signs of faulting rather than bulk failure at the grain level.

Glasses.

In the early days, silicate glass was in some ways the archetypal material for studies of brittle fracture. It was natural to test it under impact conditions also. Silicate glasses exhibit high yield strength that is associated with their amorphous state because dislocation slip is impossible in irregular structures, and low fracture toughness as a result of their high homogeneity. The fracture of glasses under compression occurs by the axial splitting. Schardin, 1959, investigated the velocity effects in fracture of glasses. Growing tensile cracks usually start with a low velocity which increases up to ultimate value as the crack propagates. Depending on the glass composition, the ultimate crack speed varies from $0.38 \cdot c_t$ (lead flint glass) to $0.61 \cdot c_t$ (fused quartz), where c_t is the shear wave speed. A surprising observation was that the rapid cracks never decelerate. If the driving stress decreases, rapid cracks either maintain speed or stop.

At high pressures brittle glasses become ductile. Ductility of glasses is caused by a loose microstructure with a large amount of molecular-size voids. It is known that glasses show gradual structural changes resulting in increased density (Arndt and Stoffer 1969). A microscopic examination of the deformed zone in glass under pyramidal indentations (Hagan 1980) shows that inelastic deformation is concentrated in shear faults of negligible thickness produced by genuine shear displacements without cracking. Once the plastic flow stars, the stress relaxation reduces the stress concentration at the crack tip and thus stops the propagation of cracks. Since the densification occurs under Vickers indentation, it is supposed (Ernsberger 1968) that the irreversible densification and compaction in the silicate structure are responsible for the plastic flow properties of glasses under high pressure. The degree of densification can be varied to some extent by variation of pressure, temperature, and shear strain, and remains irreversible under normal conditions.

Figure 18 shows a typical stress history for shock compression of a crown glass (Kanel and Molodets 1976). The dispersion of the elastic precursor wave is a result of anomalous compressibility at moderate pressures which is a property of many silicate glasses. When the

peak stress exceeds the Hugoniot elastic limit, brittle glasses become ductile. The inelastic deformation above the HEL occurs by means of the densification mechanism without cracking. Under dynamic conditions, localization of inelastic deformation is accompanied by a temperature rise within the shear bands that, in turn, should decrease the densification threshold and provide the ductility under unloading. It follows from the spall strength measurements below and above the HEL. Figure 19 shows free surface velocity profiles for K9 crown glass (Kanel et al. 1998). Spallations were not observed in these shots, which means that the spall strength of the glass exceeds 6.8 GPa below the HEL and remains very high above the HEL. For comparison, we can mention that the static tensile strength of glasses is around 0.1 GPa. The dynamic strength of glass rods exceeds the static value by a factor of ~2 (Kolsky and Shi 1958). The reason for such a large discrepancy is that the fracture nucleation sites in homogeneous glass are concentrated on the sample surface. These incident microcracks are activated and determine the strength magnitude in the static measurements and in dynamic experiments with rods. However, the spall strength measurements characterize the bulk properties of the matter.

Thus, in contrast to the behavior of quartz single crystals, the spall strength of glasses does not drop when prior inelastic compression occurs. The high spall strength revealed in the stress range above the HEL means that the ductility is preserved even following tension in the material.
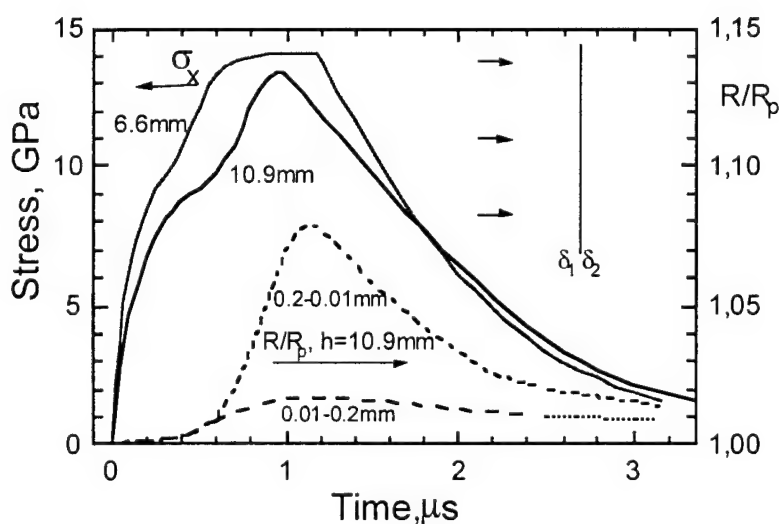
Fig. 18. Stress history in the K8 glass target impacted by a PMMA flyer plate (6 mm thickness, 3.15 km/s impact velocity). Measurements were carried out at distances of 6.6 and 10.5 mm from the impact surface with manganin and constantan gauges insulated by Teflon. Dotted lines show the component of gauge resistance increases due to gauge elongation. δ_1 is the thickness of film placed toward the impact side, δ_2 is the film thickness toward the sample rear surface.

The localization of inelastic deformation was observed by Kanel and Molodets, 1976, in the K8 crown glass under shock compression and unloading. In this study, a distortion of internal interfaces of the two-piece glass targets was revealed under uniaxial compression above the HEL. The distortion appeared in elongation of the manganin piezoresistive foil gauges used for recording the stress profiles. Figure 18 presents both the stress history and the component of gauge resistance increase that is due to the gauge elongation. The foil gauges sense the surface distortion if the non-uniformity size is comparable to or larger than the gauge foil thickness. Obviously, this finding is a result of localization of deformation which forms blocks bounded by cracks or shear bands. The distortion is also higher in the gauge next to the receiving block. A very surprising feature is the reversibility of the surface distortion, which means that the unloading strain occurs along the same shear faults that were strained under compression. Another important observation is that the maximum of the surface distortion is delayed relative to the stress maximum. Obviously, mutual shifting of blocks and, correspondingly, the shear stress relaxation are continuing until the shear stresses relax.
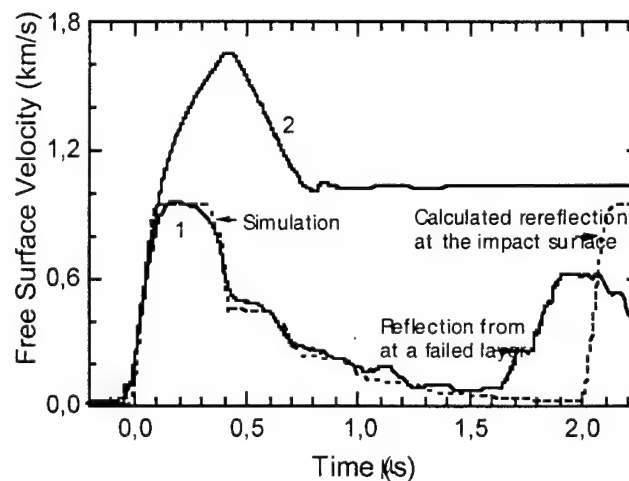
Fig. 19. Experimental results for K9 glass samples 6.1 mm thick at the impact velocities of 670±30 m/s (profile 1), and 1900±50 m/s (profile 2). Impactors are steel 0.9 mm thick (1) and aluminum 2 mm thick backed by paraffin (2). Dashed line shows results of computer simulations assuming no failure occurred.

The impact loading of a glass and, probably, other brittle materials can be accompanied by an appearance of a failure wave. The failure wave is a network of cracks that are nucleated on the surface and propagate into the stressed body. There are many observations of fracture front propagation in glasses under high tensile stresses. Schardin, 1959, recorded expansion of circular fractured areas with a sharp front formed by bifurcated cracks. He also observed detonation-like propagation of fracture in glass pipes filled with compressed gas. Chandrasekar and Chaudhri, 1994, recorded the explosive disintegration of thermally tempered glasses, the internal central region of which was under tensile stress. Galin et al., 1966, reported an explosion-like fracture under bending of high-strength glass with removed surface defects. The

30

explosion fracture resulted in formation of micrometer-size glass particles and was treated by Galin and Cherepanov, 1966, in terms of self-propagating failure wave. The similar fracture mode under compression was revealed in shock-wave experiments. We can hope that the investigations of failure wave in shock-compressed glasses provide information about the mechanisms and general rules of nucleation, growth and interactions of the multiple cracks and will help us to interpret better the experiments with other hard brittle materials, such as ceramics and rocks.

In modeling the behavior of materials subjected to intense impulsive loading, it is usually implied that local material response can depend only on characteristic material properties and the local state. In the case of cracking, the material ahead of the fracture zone should not "know" that cracks even exist. It seems the failure wave is an example of non-local behavior. The response of each elementary volume in the body depends not only on its local state, but also on whether the failure wave has approached the point of interest or not.

The failure wave was originally observed under the planar shock-wave compression below the Hugoniot elastic limit. In experiments described by Razorenov et al., 1991, and Kanel et al., 1992, the shock pulse was introduced into the glass sample through a copper baseplate. When the peak stress of the shock pulse was far below the elastic limit, a short negative velocity pullback appeared in the free-surface velocity profile as a result of the re-reflection of the rarefaction wave at the sample-baseplate interface. In contrast, however, no re-reflected tensile pulses were observed in experiments near the elastic limit. Instead, a small velocity rise was observed on the free surface profile, and the moment of this velocity rise was earlier than the elastic wave reverberation in the sample. This modification of the wave process was explained in terms of the formation of a failed layer near the sample-baseplate interface under uniaxial compression. An expansion of this failed layer was interpreted as a failure wave propagation. Bourne et al., 1997, and Kanel et al., 1998, observed re-establishing of the failure wave at inner interfaces in composed glass samples.

Brar et al., 1991, 1992, and Bless et al., 1992, have shown by direct measurements on a soda lime glass that behind the failure wave the tensile strength drops to zero, or almost to zero, and the transverse stress increases, indicating a decrease in shear strength. Figure 20 shows an example of earlier measurements of longitudinal and lateral stresses at shock compression of glass near the elastic limit made by Kanel et al., 1977, which was treated first as a delayed collapse. Figure 21 summarizes the results of stress difference measurements by Brar et al., 1991, and Kanel et al., 1977. The failure waves were recorded in the longitudinal stress range of 4 to 10 GPa; for this stress range the diagram shows the stress difference ahead and behind of the failure front. It looks quite reasonable that reduction in the final stress difference with increasing the shock intensity, and, respectively, increasing the comminution degree, occurs. At peak stresses > 10 GPa, the densification processes start in glass which provide the shear stress relaxation without cracking. Perhaps, a second rise in the stress difference at ~15 GPa is evidence of maximum densification reached.
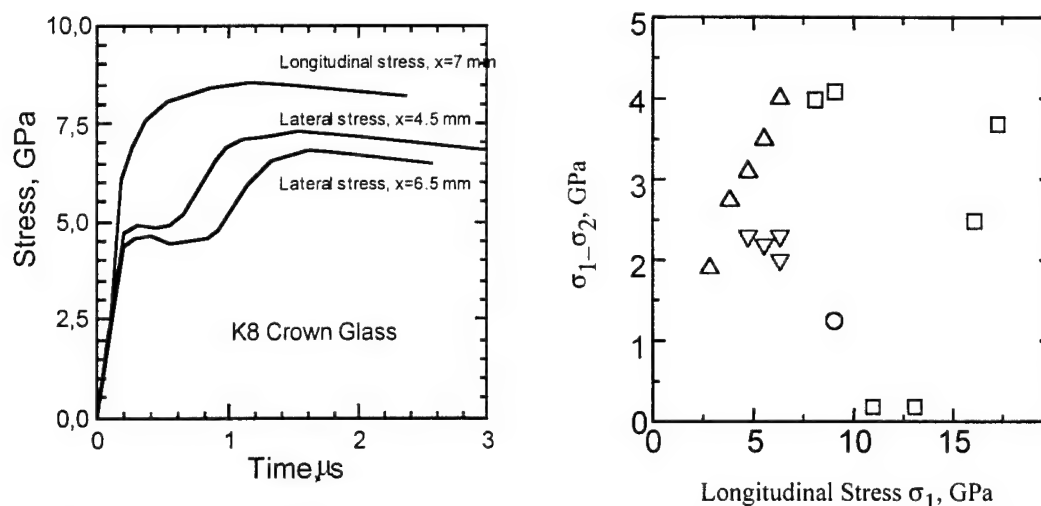
Fig. 20. (Left) Profiles of longitudinal and lateral stress in the K8 crown glass measured with manganin gauges near the HEL. The distance of wave propagation is mentioned.

Fig. 21. (Right) Results of measurements by Brar et al., 1991, (triangles) and Kanel et al., 1977, (squares and circles) of stress difference in shock compressed glass as a function of the peak stress.

Raiser and Clifton, 1994, and Raiser et al., 1994, have found that the surface roughness of the aluminosilicate glass between 0.04 and 0.52 μm does not appear to play a significant role in the formation of a failure wave. Independently on the surface roughness, they observed a high spall strength of the glass when the compressive stress was around 3.5 GPa, while at the peak stresses of 7.5 to 8.4 GPa the spall strength was high ahead of the failure front and was low behind it. They also obtained evidence of increasing of the failure wave velocity with increasing impact stress. Bourne et al., 1997, have found that deliberately introducing flaws by roughening the surface speeds the fracture of a glass, increasing the failure wave average velocity. Dandekar and Beaulieu, 1995, have found that failure wave is initiated in a soda lime glass at an impact stress between 4.7 GPa and 5.2 GPa. The propagation velocity of the failure wave is determined to be 1.56 km/s and it remained constant with the thickness of glass sample between 3.1 and 9.4 mm at the impact stress of 5.2 GPa. Espinosa et al., 1997, observed a progressive reduction in normal stress behind the failure wave close to the impact surface. They have concluded that the inelastic process responsible for the reduction in shear strength has well defined kinetics. While much work has concentrated around relatively open structure, lower density glasses, Bourne et al., 1996, and Kanel et al., 1998, observed the failure wave in a higher density filled lead glass.

Brar and Bless, 1992, Bourne and Rosenberg, 1996, and Senf et al., 1995, have visualized the failure wave. Very interesting results were obtained in experiments with large specimens of the optical glass K5 impacted by blunt steel cylinders (Senf et al. 1995). The experiments demonstrated several modes of the fracture nucleation. Around the edges of the projectile, many cracks are initiated by the propagating surface wave, which form the conical-shaped fracture zone. In the central part, the damage zone exhibits a planar front that propagates with a velocity equaling the terminal crack velocity of 1,550 m/s in this type of glass. Besides the

fracture nucleation on the sample surface, separate crack nucleation sites were also activated at the microdefects inside the stressed glass target. As a result, several spherical or nearly spherical failure waves were found to form ahead of the main front.

It would be important to explain the peculiarities of the free-surface velocity profiles when the failure wave is formed. In most of the experiments, the free-surface velocity profiles contain smooth maxima immediately behind the front. Computer simulation of the phenomenon performed by Kanel et al., 1992, and an acoustic analysis performed by Utkin (Kanel et al. 1996) showed that the "rounding" of the top of the compression wave could be formed as a result of several reasons. These include decreasing propagation velocity of the failure wave, or increasing yield strength of comminuted material, or increasing relaxation time with increasing propagation distance. Brace and Bombolakis, 1963, in their study of the growth of cracks in glass under compression, found that the cracks grow along a curved path which becomes parallel with the direction of compression. When this direction is attained, growth stops. This observation may explain the decreasing velocity of the failure wave or increasing relaxation time.

Recently, Feng, 2000, has proposed a diffusion model for the failure wave. Shear micro-fissures diffuse with a diffusivity proportional to the stress deviator behind the elastic shock. Initial results from this model are very promising.

5. DYNAMIC STRENGTH PROPERTIES OF POLYCRYSTALLINE CERAMICS

The response of ceramics has been studied by many authors, since their low densities and high Hugoniot elastic limits have made them attractive potential armor materials. Extensive studies have been conducted to obtain Hugoniot data, longitudinal wave profiles, and the spall strength data for various ceramics under shock-wave loading. The most widely tested and applied ceramics are Al_2O_3, B_4C, SiC, TiB_2, and AlN. They are densified by liquid-phase sintering, solid-state sintering, or hot pressing. The dynamic mechanical properties of these ceramics are discussed below.

Aluminum oxide.

Knowledge of the dynamic yield behavior of polycrystalline aluminum oxide (alumina) is important because of technical uses of this material. Table 1 summarizes the HEL data for Al_2O_3 ceramics in different states. Ahrens et al., 1968, reported Hugoniot data for the G.E. high density ceramic Lucalox (0.2% porosity) and a lower density ceramic Wesgo Al-995 (3.5%-4.3% porosity). The measured HEL values are 11.2±1.3 GPa for Lucalox and 8.3±0.5 GPa for Al-995 ceramics. Using the values of Poisson's ratio obtained from ultrasonic data, the yield strength was determined as 7.8 GPa and 6 GPa, respectively. Gust and Royce, 1971, performed the Hugoniot measurements for five aluminas. Whereas the general trend is in the HEL reduction with decreasing ceramic density, they have found that impurity content and

material processing also influence the HEL value. The compaction of more porous ceramics occurs within the stress range from the yield point to about 30 GPa. At the higher stresses, the states of all alumina ceramics are described by one curve in the stress-volume coordinates. Beyond the compaction region, the yield strength estimated from the stress offset between the Hugoniot and isotropic compression curve is comparable to but somewhat smaller than the yield strength at the HEL.

The profiles of shock compression and unloading waves propagating through alumina ceramics are similar to those for silicon carbide shown in Fig. 9. The compression wave exhibits an elastic jump and a subsequent dispersive rise to the plastic wave, which compresses the matter to a final state. According to measurements by Munson and Lawrence, 1979, the unloading wave front in shock-compressed alumina is elastic. There is no sharp distinction between the elastic and inelastic parts. The rounding transition from the elastic to inelastic portions of the compression wave makes it difficult to unambiguously determine the HEL value. Perhaps this is the reason there is controversy over whether aluminas exhibit precursor decay. In the case of rate-dependent response of ceramics, precursor decay should be observed.

The results of Grady's VISAR experiments on AD995 plates 2.5 to 10 mm in thickness show that, although it appears as if the precursor is decaying, a self-similar scaling plot shows that within a natural scatter there is no decay. In contrast, Yaziv et al., 1988, observed precursor decay from 6.1 to 4.7 GPa in the AD-85 ceramic when the propagation distance increased from 6.15 mm to 36.8 mm. Murray et al., 1996, also measured decay of 20 to 25% for lower density aluminas. It is necessary to note, however, that the interpretation may have been incorrect because of the limited time resolution of the manganin gauges used in these studies. On the other hand, in the case of gradual transition to inelastic compression, it is not quite clear what stress level should be identified as the HEL value, even if stress is measured with good resolution. Figure 22 shows schematically the stress-volume trajectory for a strain-hardening solid under uniaxial compression. Inelastic deformation results in deflection of the real compression curve from a purely elastic one toward smaller volumes. The real compression curve may be smooth and inflected, as shown in Fig. 22. The precursor front velocity corresponds to the slope of the Rayleigh line connecting points at initial zero-stress state and at the state on the real compression curve where the Rayleigh line is tangent to it. At the shown shape of compression curve, the inelastic deformation starts within the steady elastic precursor front at smaller stress and develops behind the front without a break in the wave profile. As a result, a rounded precursor profile is formed. With increasing propagation distance, the stress gradient behind the elastic precursor front should decrease in a self-similar manner, so with limited time resolution it appears as a decrease in the HEL value.

Thus, the stress measurements at the elastic precursor front in strain-hardening solids characterize exactly neither the onset of inelastic deformation nor the resistance to subsequent deformation. For technical applications, the yield properties of strain-hardening materials are characterized by 0.2% yield strength, which is the flow stress corresponding to the 0.2% plastic strain. Perhaps it would be reasonable to introduce a similar convention for the shock-wave tests as well. For example, one might use the stress at some particular scaled time (time divided by the distance) behind the precursor front.
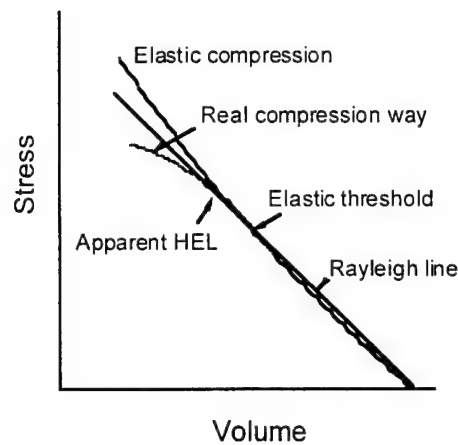
Fig. 22. The stress-volume trajectory of state of a strain-hardening solid in a course of compression in elastic precursor wave.

Cagnoux and Longy, 1988, performed VISAR free surface velocity measurements for alumina with various rise times of the compression wave entering into the sample. The HEL was found to be independent on the wave propagation distance, the peak shock stress, and the entering stress gradient; this means that there is no influence of strain rate on the yield strength of alumina in a range of $5 \cdot 10^4$ to $6 \cdot 10^5$ s^{-1}. They also carried out measurements of double-impact loading which showed that the Hugoniot elastic limit is increased by reloading as a result of strain hardening. Furnish and Chhabildas, 1998, studied the step-like compression of AD995 ceramic. Analysis of particle velocity profiles showed the second wave front propagates even faster than the elastic precursor front at stresses both below and above the HEL value. The apparent HEL value rose from 6.5 to 7.9 GPa at step-like shock loading, but even at 11 GPa the elastic front was recorded in the second compression wave that is evidence of rate-dependent behavior. Strain rate sensitivity manifests itself in the "plastic" shock rise time also.

Besides the porosity, yield strength of ceramics depends on the grain size. Longy and Cagnoux, 1989, have found that alumina ceramics with 99.7% Al_2O_3 and 2% porosity but with the grain size of 5 and 60 μm exhibit HEL of 8.5 GPa and 5 GPa, respectively. Bourne et al., 1994, from experiments on seven aluminas of 95.5% to 97.4% Al_2O_3 content and 2 to 4% porosity have found a decrease in HEL value from ~7.5±1 GPa at ~2 μm grain size to ~5±0.5 GPa at ~8 μm. Cagnoux, 1990, carried out microscopic examination of alumina samples of two different grain sizes (4.7 μm and 10-20 μm) with 99.7% Al_2O_3 content and 3.91 g/cm^3 density. The samples were recovered after compression above their HEL in spherical shock waves. In the region of maximum peak stresses the fine-grain alumina remained uncracked, whereas the coarse-grain sample was microfragmented. The SEM photographs of fine-grain samples show reduction in porosity, with no slip-nucleated microcracks; in the coarse-grained sample numerous twins were observed. It was concluded that twinning is favored by large grain size

while slipping by small grain size. Activation of additional mechanisms of inelastic deformation should reduce the yield stress.

Wang and Mikkola, 1992, observed twins in fragments of recovered shock-compressed samples of high-purity alumina with 25 μm average grain size. The defect densities in polycrystalline samples were lower than in single crystals, especially at the highest shock stress of ~23 GPa. However, at high shock stresses, single crystals show considerably less fragmentation than the polycrystals. In polycrystals, the grain boundaries serve as crack initiation sites and crack propagation paths, thus contributing to fragmentation.

Longy and Cagnoux, 1989, observed compaction in recovered porous ceramic samples at shock stresses starting from ~80% of the HEL value. This compacting was not accompanied by detectable damage in pure alumina at impact stresses up to 2 HEL. X-ray analysis showed broadening of the diffraction lines at a higher stress level as a result of microplastic strains. Some grains exhibited surface marks which indicated occurrence of microplastic deformation. Examination of impure alumina showed microcracks in the inter-granular glassy phase after shock stress 0.9 HEL and over. Microscopic examination showed no relationship between the HEL and microcracking. TEM observations revealed numerous grains which were not strained at 2 HEL. The plastic nature of the yielding during a uniaxial deformation process was attributed to the confinement imposed by this type of loading.

Figure 23 presents results of spall strength measurements as a function of normalized peak stress for alumina (Rozenberg 1992, Dandekar and Bartkowski 1994, Staehler et al. 1994, and Song et al. 1994). Besides the data shown in Fig. 23, Longy and Cagnoux, 1989, measured the spall threshold and spall strength of several aluminas at the peak stresses both below and above the HEL. The spall threshold of pure fine-grain alumina decreases from 0.5 GPa at 2% porosity to 0.3 GPa at 17% porosity. They have found that, within the experimental error, the spall strength measured from the free surface velocity profiles below the HEL is equal to the spall threshold. Even more, the measurements show the spall strength remains of the order of the spall threshold for a peak stress up to twice the HEL. At 2 to 6% porosity, the spall threshold and the spall strength above the HEL have been measured the same for 99.7 and 94% alumina content in the ceramic. Bourne et al., 1994, measured the spall strength for seven aluminas of 95.5% to 97.4% Al_2O_3 content and 3.75 to 3.85 g/cm^3 density as the grain size varied from 2 to 8 μm. The spall strength measure at ~0.4 HEL varies from 0.3 to 0.6 GPa with a general trend to decrease with increasing porosity, which was varied from 2 to 4%, and increasing grain size. According to their data, the glassy phase reduces the spall strength.

Table 1. Hugoniot elastic limits of aluminas.

| Material	Density, g/cm³, (Porosity, %)	Longitudinal Sound Velocity, c_l, km/s	Poisson's Ratio	Hugoniot Elastic Limit, GPa	Dynamic Yield Strength, Y, GPa	References
Lucalox 99.8% Al_2O_3	3.98 (<0.2)	10.95	0.2363	11.2±1.3	7.8	Ahrens, Gust, and Royce, 1968
Lucalox 99.9% α-Al_2O_3 25-40 μm grain size	3.969	10.92		9.1±0.4	6.0	Munson and Lawrence, 1979
MTU JS-I, 99.99% alumina, 1.5 μm grain size	3.974	10.9	0.237	11-11.9	7.6-8.2	Staehler et al., 1994
D999, 99.9% alumina, 4 μm grain size	3.99	10.82	0.232	13-14	9-9.8	Murray et al., 1996
Carborundum Hot pressed	3.92 (0.8)	10.59	0.243	9.2-16		Gust and Royce, 1971
Wesgo Al-995 99.5% Al_2O_3	3.81 (3.5-4.3)	10.2	0.218	8.3±0.5	6.0	Ahrens, Gust, and Royce, 1968
D975 97.5% alumina, 4 μm grain size	3.8	10.3	0.234	7.5-9	5.2-6.2	Murray et al., 1996
Coors AD995 alumina with aluminosilicate glass	3.88 (2)	10.56		6.7±0.1		Dandekar and Bartkowski, 1994
Coors AD995	3.89	10.59	0.234	6.2±0.4	4.3	Grady, 1994
Coors AD-85	3.42 (6.6)	8.84	0.256	6.1-6.5		Gust and Royce, 1971
Coors AD-85, 84% alumina	3.42 (6.6)			4.7-6.1		Yaziv et al., 1988
H880 88% alumina, 2 μm grain size	3.55	9.1	0.226	5.5-6.5	3.9-4.6	Murray et al., 1996
Diamonite P-3142-1	3.72 (5.5)	9.98	0.234	7.2-8.1		Gust and Royce, 1971
Desmarquest alumina	3.62 (5.3)	9.45		4.5		Cagnoux and Longy, 1988
ENSCI alumina, 4.7 μm grain size	3.91 (2)	10.63		8.7±0.4		Longy and Cagnoux, 1989
ENSCI alumina 1 μm grain size	3.54 (11)	9.34		5		Longy and Cagnoux, 1989
ENSCI alumina 0.6 μm grain size	3.31 (17)	8.55		4-5		Longy and Cagnoux, 1989
ENSCI T60, 99.7% alumina, 5-125 μm grains	3.85 (3.5)	10.32		5		Longy and Cagnoux, 1989
UL500, 93.8% alumina, 11 μm grain size	3.62 (6.2)	9.77		6.5		Longy and Cagnoux, 1989
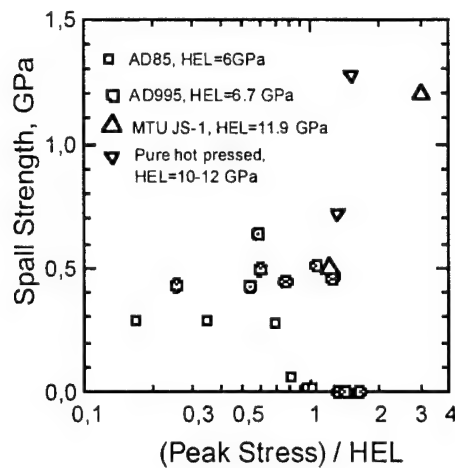
Fig. 23. Spall strength of alumina ceramics as a function of peak stress. Data for AD85 from Rosenberg, 1992; for AD995 from Dandekar and Bartkowski, 1994; for hot pressed pure alumina from Staehler et al., 1994, and Song et al., 1994.

Thus, the spall strength of alumina depends on porosity and, probably, the material grain size in the same way that tensile strength under quasi-static tension does. It seems the spall strength undergoes a transition, first decreasing near the HEL, then increasing with increasing pressure above the HEL. The reduction in spall strength value near the HEL is especially significant for aluminas with a large glassy phase content. This observation correlates with microcracks in the inter-granular glassy phase after shock stress of 0.9 HEL and over observed by Longy and Cagnoux, 1989. Yeshurun, Staehler et al., 1994, attributed transition in the spall strength variation with the peak stress to a change in the dominant inelastic deformation mechanism from microcracking near the HEL to dislocation activities at higher peak stresses.

Bourne et al., 1998, observed features of the lateral stress traces in alumina 975 that were similar to failure waves in glasses. The measurements were done at peak stress around the HEL value. The lateral stress traces measured near the impact surface show an initial plateau at 3 GPa followed by a rise to a second higher value of ~4.5 GPa. At 5 mm and deeper into the target no failure wave was seen to arrive. They also recorded the reloading signal in the free surface velocity profile for alumina 999 which is considered as failure wave evidence too. If the appearance of failure waves in ceramics is confirmed by other data, such as the spall strength measurements at different distances from the impact surface, the finding will mean that the surface layers of ceramic tiles contain many more potential crack nucleation sites than the matter inside the tile. Although the systematic spall strength measurements at different distances have not been done yet, we may mention that Munson and Lawrence found zero strength of shock compressed Lucalox at peak stresses right at the HEL and above it in their experiments with impactor and target thicknesses of 5.04 mm and 6.35 mm, respectively. Other aluminas, except AD-85, do not exhibit zero spall strength in the vicinity of the HEL.

In the rod impact experiments (1-D stress conditions), Bless et al., 1990, have found the failure threshold of 2.7 GPa for AD94 and 4 GPa for AD998. Wise and Grady, 1994, performed the impact experiments with confined and unconfined rods of AD995 alumina. For unconfined rods at impact velocities of 1 and 2 km/s, they have found the same maximum axial stress of 3.15 GPa at a distance of eight rod diameters. This stress magnitude may be considered as the failure threshold, which is lower than the dynamic strength of 4.3 GPa at the HEL for this material. For the alumina rods mounted within a close-fitting Ta sleeve, the maximum axial stress was 5.8 to 6.3 GPa. This increase in stress-wave amplitude with increased confinement was consistent with expectations of approaching an upper dynamic limit equal to the HEL of the AD995 alumina (6.2 GPa). Besides the longitudinal velocity history, they measured also the transversal velocity component which can be useful for computer simulations of the material behavior. Chhabildas et al., 1998, performed experiments with confined and unconfined AD995 alumina rods gradient-density impactors. A time-dependent stress pulse generated by such an impactor allows an efficient transition from the initial uniaxial strain loading to a uniaxial stress state as the stress pulse propagates through the rod. As a result, they observed an increase in the maximum axial stress in unsleeved rods from 3.4 GPa when a single-density impactor was used to 3.5-4.2 GPa with a graded-density impactor. For the rod confined in a steel sleeve, the maximum axial stress was 4.6 GPa.

Lankford et al., 1998, discussed the behavior of Al_2O_3 under compressive loading over a wide range in strain rate and degrees of confinement. They concluded that the ceramics do experience multi-slip system plastic flow under compressive loading at all strain rates if the yield point can be obtained earlier than fracture occurs. Generally, a confinement prevents premature failure via microfracture. In the high-purity fine-grain alumina with extremely clean grain boundaries, the plastic limit probably can be reached even without confinement.

Silicon carbide.

The lightweight intermetallic compounds are characterized by large dynamic impedances and large yield strength. Gust et al., 1973, measured the Hugoniot of hot-pressed silicon carbide ceramic. They have found that SiC exhibits evidence of very sluggish phase transition or a phase transition with a small volume change. However, subsequent measurements of the shock-wave profiles at 27.6 GPa and 36.5 GPa peak stress made by Kipp and Grady, 1990, as well as measurements of hydrostatic compressibility in a diamond anvil cell by Bassett et al., 1993, have not confirmed this finding. The hydrostatic data have been described up to 68.4 GPa by the Birch-Murnagan equation with a bulk module K_0=230.2$\pm$4.0 GPa and K_0'=4.

Table 2 presents results of measurements of the Hugoniot elastic limits of silicon carbide ceramics. The HEL values obtained through the particle velocity profile measurements exceed the value reported by Gust et al., 1973. It is speculated that this is due to the substantially lower silica content of modern silicon carbides. Post-yield strength of silicon carbide, determined by comparison of Hugoniot uniaxial strain and calculated hydrodynamic response, reveals significant strengthening with subsequent deformation beyond the initial dynamic yield. According to Grady, 1992, the maximum shear stress in Eagle-Picher SiC ceramic increases from 7 GPa at the

HEL to 10 GPa at ~30 to 50 GPa shock stress. The release trajectories for silicon carbide indicate reverse yielding and continued strength characteristics of elastic-plastic material behavior, probably with a Baushinger effect at higher peak stresses. According to Feng et al., 1998, the maximum shear stress in the Cercom SiC-B hot-pressed ceramic increases from 4.5 GPa at the HEL to 7.0 GPa at a shock stress approximately twice the HEL.

Table 2. Hugoniot elastic limits of silicon carbide ceramics.

Material	Density, g/cm³, (Void fraction, %)	Longitudinal Sound Velocity, c_l, km/s	Poisson's Ratio	Hugoniot Elastic Limit, GPa	Dynamic Yield Strength, Y, GPa	References
Carborundum Co., type KT, 99.2% SiC	3.09 (4)	11.4	0.157	8±3	6.5	Gust, Holt, and Royce, 1969
Eagle-Picher α-SiC, 7 μm grain size	3.177 (1)	12.06	0.16	15-16		Kipp and Grady, 1990
Cercom type B hot-pressed, 99.3% SiC, 2 μm grain size	3.221	12.22	0.164	11.7		Feng et al., 1998
Reaction bonded, 1.2 μm grain size, 4.5 GPa static comp. strength	3.21	11.89	0.18	13.2±0.3	10.4	Bourne and Millett, 1997
Sintered, 4.5 μm grain size, 5.2 GPa static comp. strength	3.16	11.94	0.16	13.5±0.3	11	Bourne and Millett, 1997
Hot pressed, 2.9 μm grain size, 5.2 GPa static comp. strength	3.24	12.34	0.17	15.7±0.3	12.6	Bourne and Millett, 1997

Figure 24 summarizes the results of spall strength measurements at varied peak stress. As in the case of alumina, the results are very scattered and show a tendency to decrease when the peak stress is in a vicinity of HEL. However, there is no evidence that the spall strength falls to zero at the HEL. Bartkowski and Dandekar compared the spall properties of sintered and hot pressed silicon carbide under the same test conditions. The results demonstrate that hot pressed ceramic has better cohesion between grains than the sintered material.

Pickup and Barker, 1998, made split Hopkinson pressure bar experiments at the strain rate of ~10^3s^{-1} with three SiC ceramics which were manufactured in different ways: produced from a reaction bonding technique, pressureless sintered, and made from a pressure assisted densification method. The measured dynamic compressive strength is 6.7 GPa, 7.5 GPa, and 8.2 GPa, respectively, whereas the quasistatic compressive strength of these materials is 4.5 GPa, 5.2 GPa, and 5.2 GPa, respectively. The first material failed in an apparently brittle behavior, while the others demonstrated a significant period of apparently inelastic flow. For the second (sintered)

material, they also observed ejection of failed microparticles from the sample surface which initiated at stress around the quasistatic failure strength. For the third (hot pressed) material, there was no evidence of any ejecta being formed from exceeding the quasistatic compressive strength up to the attainment of the highest stress. The ranking of relative resistance to damage in the SHPB experiments correlates with the results of shear strength measurements under shock compression made for the same three ceramics. Bourne and Millett, 1997, found hardening of hot pressed SiC over an applied longitudinal stress range of ~1 to 1.4 times the HEL, whereas the shear strength of two other SiC ceramics softened over the same stress range.

The lateral stress profiles measured by Bourne and Millett, 1997, indicate that above the HEL the failure of SiC ceramics was delayed for some time after the maximum stress had been achieved. The finding was interpreted in terms of the failure wave phenomena.
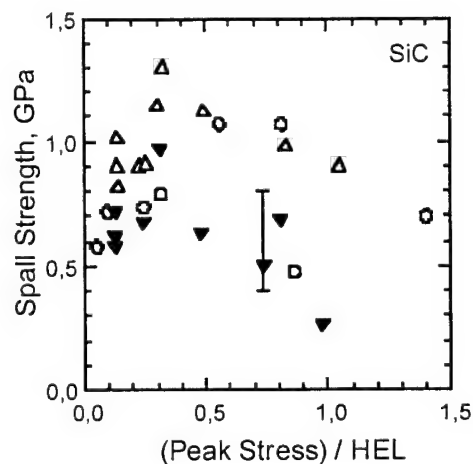
Fig. 24. Spall strength of silicon carbide ceramics vs. impact stress. Bar shows data by Grady, 1992, and Kipp and Grady, 1992 for Eagle-Picher SiC; circles are data by Winkler and Stilp, 1992, triangles show data by Bartkowski and Dandekar, 1996, for hot-pressed Cercom SiC-B, 2 μm grain size (open triangles) and sintered Sohio SiC, 15 μm grain size (solid triangles).

Boron carbide.

Fig. 9 shows a typical wave structure in boron carbide measured by Kipp and Grady, 1990. The inelastic deformation behind the precursor front is accompanied by a dramatic loss in strength supporting capability. This is exhibited by the precursor shape and by the subsonic velocity of the second compression wave. According to Grady, 1992, Hugoniot and hydrodynamic response for boron carbide converge at stresses approaching about twice the HEL. A dispersive character of the unloading wave indicates that the amplitude of elastic unloading is very small. The stress-strain trajectory for the B_4C ceramic shows evidence of dilatancy when the compressive stress approaches zero on unloading.

The velocity profiles for boron carbide, as well as stress histories measured by Brar et al., 1992, show instabilities behind the elastic precursor front. In experiments with a gapped flat mirror, Mashimo and Uchino, 1997, observed jagged profiles of the moving free surface both in the elastic and plastic region. An average period of the nonuniformities formed on the B_4C sample surface was of order of 1 mm, a maximum local displacement was a few tens of μm. Such a heterogeneous free surface motion is evidence of operating macroscopic slip systems, such as cracks, cleavages, and melting zones.

Brar et al., 1992, measured the HEL values for B_4C ceramics of different porosity and the same grain size. They have found the HEL decreases with porosity according to the relationship

$$\sigma_{HEL}^p = (Z_p/Z_s)^2 \sigma_{HEL}^s$$

where σ_{HEL}^p and σ_{HEL}^s are the Hugoniot elastic limit of the porous and solid matter, and Z_p and Z_s are impedances of the porous and solid matter, respectively. When the porosity exceeded ~10% the elastic precursor wave shape changed: a ramped rise appeared behind the precursor front in porous ceramics instead of a spike observed at higher density. The experimental data on the Hugoniot elastic limits of boron carbide ceramics are summarized in Table 3. According to Winkler and Stilp, 1992, the spall strength of boron carbide is within a range of 0.6 to 0.8 GPa at the peak stresses up to 11 GPa, although at a higher strain rate Kipp and Grady, 1992, observed much larger spall strength of 1.8 GPa within this peak stress range. Above the HEL the spall strength of B_4C is presumed to be zero.

Titanium diboride.

Figure 25 shows the shock wave profile in a TiB_2 ceramic plate measured by Kipp and Grady, 1990. The material exhibits significant compression-wave dispersion to at least 50 GPa. The structure of the compressive wave caused difficulty in unambiguously selecting a particle velocity corresponding to the HEL. There are two smoothed breaks at ~160 m/s and ~430 m/s which correspond to ~5 GPa and ~13.5 GPa, respectively. Actually this wave structure in TiB_2 ceramic is not well reproduced. At the same impact parameters, Winkler and Stilp, 1992, recorded the free surface velocity profiles without the second break and, in one shot, with the second break at 9 GPa stress level. In the shot where the second HEL was observed, the grain size of the ceramic was much less than in others (5-10 μm and 30-50 μm, respectively). Also, the samples had different kinds of incident porosity: intergrain pores localized mainly in triple grain junctions in the case of fine-grain ceramic and mainly intragrain pores in other ceramics. The appearance of plastic defects in recovered samples has been found to be connected with stresses exceeding the second HEL. Microscopic examination of the recovered TiB_2 samples by Ewart and Dandekar, 1994, indicated that the average number density of cracks and the average crack length increase with increasing peak compressive stress. The largest generation of new cracks occurs when the peak stress exceeds the lower Hugoniot elastic limit. The damage in the form of cracking was homogeneous throughout the body.

Table 3. Hugoniot elastic limits of boron carbide ceramics.

Material	Density, g/cm^3, (Void fraction, %)	Longitudinal Sound Velocity, c_l, km/s	Poisson's Ratio	Hugoniot Elastic Limit, GPa	Dynamic Yield Strength, Y, GPa	References
Norton Co., Hot pressed, 99.7% B$_4$C	2.5 (0.8)	13.78	0.188	15.4±1	11.9±0.5	Gust and Royce, 1971
B$_4$C, 10 µm grain size	2.516	14.04	0.164	14-14.8	13.7	Kipp and Grady, 1990
Dow Chemical, 3 µm grain size	2.506 (1)	14.03	0.17	18-20	15.1	Grady, 1994
Dow Chemical, 2.5 µm grain size	2.52	13.42	0.17	19.4		Brar et al., 1992
Dow Chemical, 2.5 µm grain size	2.43	13.02	0.18	17.1		Brar et al., 1992
Dow Chemical, 2.5 µm grain size	2.33	12.8	0.18	16.3		Brar et al., 1992
Dow Chemical, 2.5 µm grain size	2.25	12.52	0.18	13.5		Brar et al., 1992
Dow Chemical, 2.5 µm grain size	2.13	11.85	0.17	9.6		Brar et al., 1992
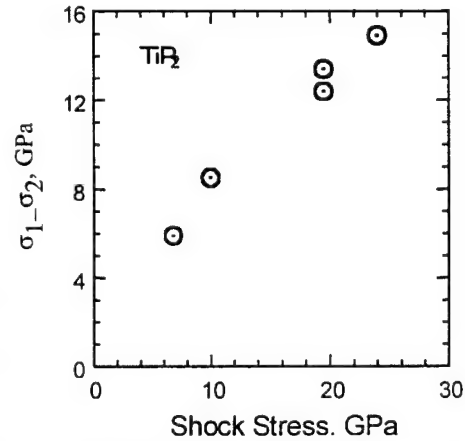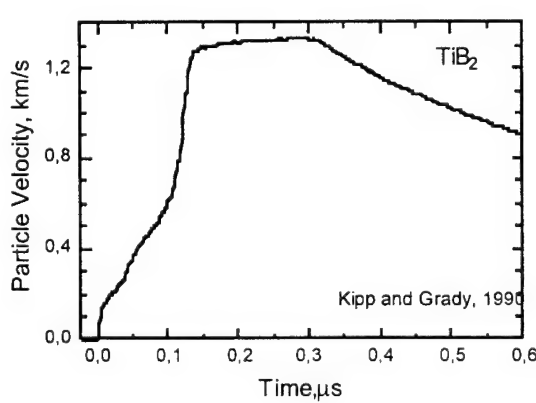
Fig. 25. (Left) Particle velocity history measured by Kipp and Grady, 1990, at the interface between titanium diboride sample plate and LiF window.

Fig. 26. (Right) Difference in principal stresses (σ_1-σ_2) as a function of peak shock stress in TiB$_2$ ceramic (Rosenberg et al. 1992).

Table 4 summarizes the results of measurements of the Hugoniot elastic limits for the titanium diboride ceramics. Rosenberg et al., 1992, measured the transverse stresses in shock-compressed TiB$_2$ ceramic. The results presented in Figure 26 show that the shear strength of TiB$_2$ at a shock stress of 24 GPa increases to more than twice its value at the lower HEL. Dandekar, 1994, calculated the shear sustained by TiB$_2$ from the stress offset between the normal shock stress and calculated hydrostat curve; he found good agreement with the data shown in Fig. 26. On the other hand, the stress-strain load-release trajectories calculated by Kipp and Grady,

43

1990, do not demonstrate as large hysteresis as could be expected with so much hardening. Figure 27 presents the results of spall strength measurements. The dramatic rise in crack lengths and densities at HEL1 observed by Ewart and Dandekar, 1994, indicates that the first HEL is a threshold above which there is increased generation of irreversible damage. The result is a falling spall threshold.
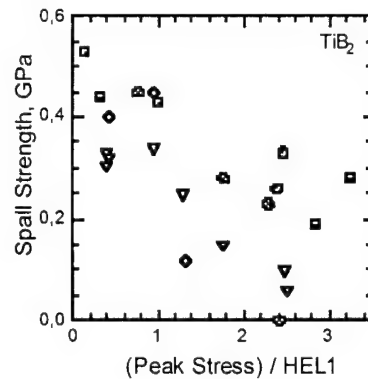
Fig. 27. Spall strength of titanium diboride ceramics vs. impact stress. Diamonds show data by Grady, 1992; circles are data by Winkler and Stilp, 1992; triangles show data by Dandekar, 1994. The peak stresses are normalized by the lower Hugoniot elastic limit of 4.2 to 7 GPa.

Table 4. Hugoniot elastic limits of the titanium diboride ceramics.

Material	Density, g/cm^3, (Void fraction, %)	Longitudinal Sound Velocity, c_l, km/s	Poisson's Ratio	Lower and upper Hugoniot elastic limits, GPa	Dynamic Yield Strength, Y, GPa	References
Union Carbide, Hot pressed, 98.5%TiB$_2$	4.51 (0)	11.21	0.141	8.6±3	7.2	Gust, Holt, Royce, 1973
TiB$_2$, 12 μm grain size	4.452	10.93	0.1	4.7-5.2 (13.1-13.7)	4.2-4.6 (11.7-12.2)	Kipp and Grady, 1990
Hot pressed, 5-10 μm and 30-50 μm grain size	4.36	10.79		4.2-4.9 (9)		Winkler and Stilp, 1992
Ceradyne, hot pressed, 98.9% TiB2, 10 μm grain size	4.49 (1)	11.23±0.21	0.1144	5.8±0.2 (13±0.4)		Dandekar and Gaeta, 1992

Aluminum nitride.

The published shock-wave data for the aluminum nitride ceramics are presented in Table 5 and Figure 28. At shock compression above 20-22 GPa peak stress, a phase transition, presumably wurtzite to rocksalt, occurs. As a result, the plastic shock wave is split in two, or

44

perhaps three, steps. The 20% volume strain associated with the transition leads to a rapid attenuation of the peak wave amplitude (Grady 1998). Measurements by Brar et al., 1992, of the longitudinal and transverse stresses in shock-compressed AlN ceramic show some moderate strain hardening which was observed also in quasistatic compressive tests under confining pressure (Heard and Cline 1980).

According to Heard and Cline, 1980, a transition from brittle to ductile inelastic compression in the hot-pressed AlN ceramic occurs at 0.5 GPa confining pressure, which is much less than the transition pressure for alumina. At the confining pressure of 0.8 GPa, the quasistatic yield strength for AlN reached 4.7 GPa, whereas without confinement it was 3.2 GPa. Microscopic examination confirmed the change in mechanical response of AlN at high pressure due to intracrystalline slip by dislocation generation and motion. Chen and Ravichandran, 1996, observed increase in compressive strength of sintered AlN by approximately 1.5 GPa as the strain rate had been increased from $4 \cdot 10^{-4}$ to $5 \cdot 10^{2}$ s^{-1}, so at the confining pressure of 230 MPa and high strain rate the strength exceeded 5 GPa. A comparison of these data with dynamic yield strength data in Table 5 suggests a ductile behavior of the ceramic under shock-wave compression.

Table 5. Hugoniot elastic limits of the aluminum nitride ceramics.

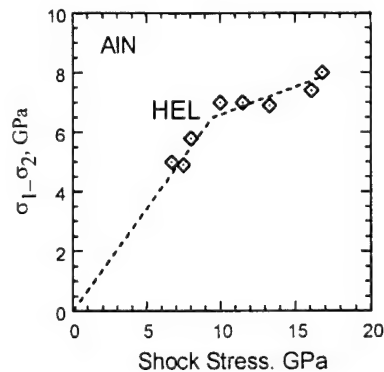| Material	Density, g/cm^3, (Void fraction, %)	Longitudinal Sound Velocity, c_l, km/s	Poisson's Ratio	Hugoniot elastic limit, GPa	Dynamic Yield Strength, Y, GPa	References
Dow Chemical, hot pressed, 2 μm grain size	3.226 (1)	10.72	0.238	9.4±0.2	6.4	Brar et al., 1992.
Dow Chemical, sintered, 4-6 μm grain size	3.20 (1-2)	10.45	0.237	7.0±0.4	4.8	Brar et al., 1992.
AlN	3.254	10.73	0.234	7.9	5.5	Grady, 1994

Fig. 28. Difference in principal stresses (σ_1-σ_2) as a function of peak shock stress in the hot pressed aluminum nitride ceramic (Brar et al. 1992).

45

Other ceramic materials.

Table 6 presents the yield strength data for some other ceramics which have not been as thoroughly investigated.

Table 6. Hugoniot elastic limits of ceramics.

Material	Density, g/cm^3, (Void fraction, %)	Longitudinal Sound Velocity, c_l, km/s	Poisson's Ratio	Hugoniot elastic limit, GPa	Dynamic Yield Strength, Y, GPa	References
BeO	2.84 (5.6)	11.54	0.198	8.2±1	6.2±0.5	Gust and Royce, 1971
Be$_4$B	1.98 (1.5)	12.42	0.094	7.4±1	6.6	Gust, Holt, and Royce, 1973
Si$_3$N$_4$	3.15	10.66		12.1		Nahme et al., 1994
Si$_3$N$_4$	2.28	8.6		1.9		Nahme et al., 1994
ZrO$_2$	5.602	6.61	0.299	5.0-5.4	3.2	Kipp and Grady, 1990
ZrO$_2$	5.954	6.87	0.306	13.2	7.4	Grady, 1994
ZrO$_2$	6.028	7.11	0.311	16.2	8.9	Grady, 1994

6. DISCUSSION

While the rod impact and Hopkinson bar experiments permit a fairly confident judgment as to whether failure is brittle or ductile, interpretation of the shock-wave experiments is more ambiguous. After the first measurements of Hugoniots for brittle materials, it was believed that the reduction in stress offset between the Hugoniot and the hydrostat was evidence for brittle fracture under shock compression. However, such behavior is not a property of brittle materials only. As an example, Figure 29 shows the shock-wave profile for zinc single crystals (Razorenov et al. 1998) which qualitatively is very similar to that measured for B$_4$C ceramic. The elastic precursor is spike-like, which is evidence for stress relaxation, implying that softening is a result of the high-rate deformation. Similar wave structure was recorded by Arnold, 1992, for Armco-iron. It was shown also that at low peak stresses the second (plastic) shock wave in Armco-iron propagates with a subsonic speed as a result of the matter softening. Figure 30 shows an experimental free-surface velocity history of Ti-6Al alloy compared with computer simulations using well-known simple models. The ramped rise behind the elastic precursor front indicates strain hardening. However, the experimental velocity profile at unloading is situated between the free-surface velocity histories for elastic-plastic and elastic-isotropic bodies, which means a partial softening of the material occurred behind the shock wave. In spite of the reduction in shear strength, all metals remain uncracked and keep their high resistance to tensile fracture.
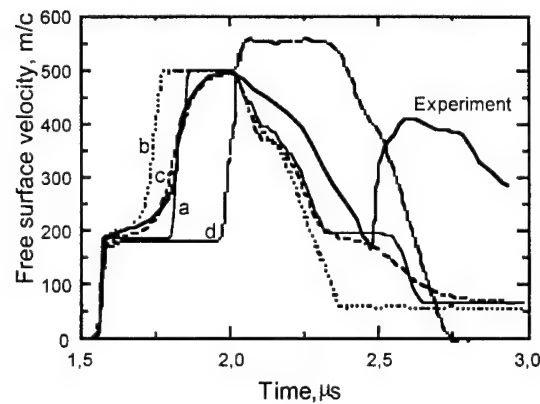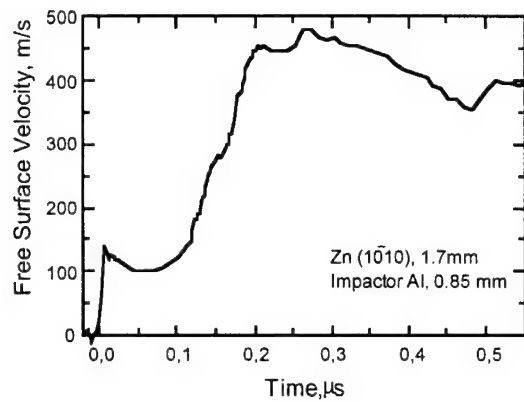
Fig. 29. (Left) The free surface velocity history for zinc single crystal impacted by Al flyer plate.

Fig. 30. (Right) Results of computer simulations of the impact loading of Ti-6%Al-4%V samples. The free-surface velocity profile "a" has been calculated using a model of an ideal elastic-plastic body. Profile "b" is the result of simulation for a strain-hardening elastic-plastic body; profile "c" is the result of simulation for an elastic-viscous-plastic body; and profile "d" is the result of simulation for an elastic-isotropic body. The thick line presents the experimental data.

Thus, the Hugoniot data and the shock-wave profiles are not sufficient to make definite conclusions about ductile or brittle response. The spall strength measurements confirm that the mode of deformation is mainly ductile as long as the observed spall strength is not zero. Note that it is possible to account for the decrease in spall strength frequently observed when the shock stress exceeds the HEL: if the peak stress does not exceed the elastic limit, the longitudinal and transversal stresses are of the same sign for the whole cycle of compression and unloading. However, if yielding occurs a hysteresis in the stress path trajectory will appear. As a result, the eventual spall may occur under a tensile longitudinal stress and a compressive transverse stress. According to Nemat-Nasser and Horii, 1982, as discussed above, such loading conditions should promote growth of cracks oriented perpendicular to the load direction.

Since the longitudinal sound velocity decreases when cracking occurs, the unloading wave speed should also be analyzed from this view point. The failure wave is also certain evidence of brittle response within the stress state range given. However, the experiments with glasses show

47

that, depending on the stress level, a material may exhibit brittle or ductile behavior even under the same uniaxial strain loading conditions. It is important to understand the mechanism of failure wave propagation under compression. According to the analysis by Nemat-Nasser and Horii, 1982, the axial crack length in compression under confining pressure should be comparable with the size of the incident inclined crack. We may suppose the depth of the damaged surface layer of glass or ceramic samples is within a range of a few micrometers to a few tens micrometers, while the failure wave propagation distance can be a few millimeters at least. Although in the static compression test the axial splitting of glass blocks may propagate on much larger distances, it is difficult to understand how such kind of cracking may provide the shear stress relaxation.

It seems an inelastic deformation under shock wave loading may occur by two mechanisms: cracking or plastic slip. Under one-dimensional strain conditions the lateral stress component is $\sigma_2 = \sigma_1 \nu/(1-\nu)$. For rigid ceramics with a small Poisson's ratio, ν, the lateral stress component is much less than the longitudinal stress σ_1. In other words, the confining pressure in plane shock waves is not very high at the HEL stress level. However, any inelastic strain increases the σ_2/σ_1 ratio, which means an elevation of the confining pressure, which may suppress cracking and create the possibility of continued inelastic deformation in a ductile mode. If strain hardening increases the flow stress too much, cracking becomes more favorable again.

To estimate the strain rate contribution to resistance to inelastic deformation, the yield strength, Y, determined from the Hugoniot elastic limit, is compared with the failure stress values measured in 1D stress conditions (quasistatic tests, Hopkinson bars, rod impact) using yielding criterion. The jump associated with transition from 1D stress to 1D strain is often associated with a kinetic-controlled response at strain rates $> (10^3\text{-}10^4 s^{-1})$. However, measurements of the Hugoniot elastic limit at different propagation distances do not demonstrate as much relaxation as should be observed in the case of high strain-rate sensitivity. Rosenberg, 1993, 1994, has suggested the use of Griffith's failure criterion for reconciliation of 1D stress and 1D strain data instead of yield criteria which are commonly used for ductile metals. In this case, the HEL should be

$$\sigma_{HEL} = (1-\nu)Y_c / (1-2\nu)^2,$$

where Y_c is the compressive strength under 1D stress conditions. Thus, Griffith's failure criterion gives the HEL strength higher by a factor of $1/(1-2\nu)$ than the yield criteria used for ductile materials and much reduces the discrepancy between the 1D stress and 1D strain data. In many cases, the Griffith's failure criterion provides very good agreement between 1D stress and 1D strain dynamic data. In effect, we may use this criterion to deduce whether the shock-wave inelastic deformation starts in ductile or brittle mode: when 1D strain data are consistent with 1D stress data, then shock failure is brittle, and it is ductile if there is disagreement.

Acknowledgment

References

Ahrens, T.J., Gust, W.H., and Royce, E.B. (1968). Material strength effect in the shock compression of alumina. *J. Appl. Phys.*, **39**(10), 4610-4616.

Anan'in, A.V., Breusov, O.N., Dremin, A.N., Pershin, S.V., Rogacheva, A.I., and Tatsii, V.F. (1974). The effect of shock waves on silicon dioxide: I. quartz. *Combustion Explosive and Shock Waves*, **10**, 372.

Arndt, J. and Stoffer, D. (1969). Anomalous changes in some properties of silica glass densified at very high pressures. *Phys. and Chem. of Glasses*, **10**(3), 117-134.

Arnold, W. (1992). Influence of twinning on the elasto-plastic behavior of Armco-iron. In: *Shock Compression of Condensed Matter 1991*. Eds.: S.C. Schmidt, R.D. Dick, J.W. Forbes and D.G. Tasker. Els. Sc. Publ. B.V., 539-542.

Asay, J.R., Chhabildas, L.C., and Dandekar, D.P. (1980). *J. Appl. Phys.*, **51**(9), 4774.

Asay, J.R. and Barker, L.M. (1974). Interferometric measurement of shock-induced internal particle velocity and spatial variations of particle velocity. *J. Appl. Phys.*, **45**(6), 2540-2546.

Ashby, M.F. and Sammis, C.G. (1990). The damage mechanics of brittle solids in compression. *PAGEOPH*, **133**(3), 490-521.

Barker, L.M. and Hollenbach, R.E. (1970). Shock-wave studies of PMMA, fused silica, and sapphire. *J. Appl. Phys.*, **41**, 4208-4226.

Barker, L.M. and Hollenbach, R.E. (1972). Laser interferometer for measuring high velocities of any reflecting surface. *J. Appl. Phys.*, **43**, 4669.

Bartkovwski, P. and Dandekar, D.P. (1996). Spall strength of sintered and hot pressed silicon carbide. *In: Shock Compression of Condensed Matter - 1995*. Eds.: S.C. Schmidt and W.C. Tao. *AIP Conference Proceedings*, **370**, 535-538.

Bassett, W.A., Weather, M.S., and Wu, T.C. (1993). Compressibility of SiC up to 68.4 GPa. *J. Appl. Phys.*, **74**(6), 3824-3826.

Bless, S.J., Brar, N.S., and Rosenberg, Z. (1990). Failure of ceramic and glass rods under dynamic compression. In: *Shock Compression of Condensed Matter 1989*. Eds.: S.C. Schmidt, J.N. Johnson and L.W. Davison. Els. Sc. Publ. B.V., 939-942.

Bloomquist, D.D. and Sheffield, S.A. (1983). Optically recording interferometer for velocity measurements with subnanosecond resolution. *J. Appl. Phys.*, **54**, 1717.

Bombolakis, E.G. (1973). Study of the brittle fracture process under uniaxial compression. *Tectonophysics*, **18**, 231-248.

Bourne, N.K., Rozenberg, Z., Grouch, I.G., and Field, J.E. (1994). Microstructural variations in seven aluminas and their effect on impact response. In: *High-Pressure Science and Technology - 1993*. Eds.: S.C. Schmidt, J.W. Shaner, G.A. Samara and M. Ross. *AIP Conference Proceedings*, **309**, 769-772.

Bourne, N.K., Millett, J.C.F., and Rosenberg, Z. (1996). Failure in a shocked high-density glass. *J. Appl. Phys.*, **80**(8), 4328-4331.

Bourne, N.K., Millett, J.C.F., and Rosenberg, Z. (1997). On the origin of failure waves in glass. *J. Appl. Phys.*, **81**(10), 6670-6674.

Bourne, N.K. and Millett, J.C.F. (1997). Delayed failure in shocked silicon carbide. *J. Appl. Phys.*, **81**(9), 6019-6023.

Bourne, N.K. and Rosenberg, Z. (1996). The dynamic response of soda-lime glass. In: *Shock Compression of Condensed Matter - 1995*. Eds.: S.C. Schmidt and W.C. Tao. *AIP Conference Proceedings*, **370**, 567-572.

Bourne, N.K., Rosenberg, Z., and Field, J.E. (1998). Surface fracture zones in shock-loaded polycrystalline ceramics. In: *CP429, Shock Compression of Condensed Matter – 1997*. Eds.: S.C. Schmidt, D.P. Dandekar and J.W. Forbes. *AIP Conference Proceedings*, **429**, 493-496.

Brace, W.F. and Bombolakis, E.G. (1963). A note on brittle crack growth in compression. *J. Geophys. Res.*, **68**, 3709-3713.

Brace, W.F., Paulding, B.V., and Scholz, C. (1966). Dilatancy in the fracture of crystalline rocks. *J. Geophys. Res.*, **71**, 3939-3953.

Brannon, P.J., Morris, R.W., Konrad, C.H., and Asay, J.R. (1984). Shock-induced luminescence from X-cut quartz and Z-cut lithium niobate. In: *Shock Waves in Condensed Matter – 1983*. Eds.: J.R. Asay, R.A. Graham and G.K. Straub. Elsevier Science Publishers B.V., 303-306.

Brar, N.S., Bless, S.J., and Rozenberg, Z. (1991). Impact-induced failure waves in glass bars and plates. *Appl. Phys. Lett.*, **59**(26), 3396-3398.

Brar, N.S. and Bless, S.J. (1992). Failure waves in glass under dynamic compression. *High Pressure Research*, **10**, 773-784.

Brar, N.S., Bless, S.J., and Rozenberg, Z. (1992). Response of shock-loaded AlN ceramics determined with in-material manganin gauges. In: *Shock-Wave and High-Strain-Rate Phenomena in Materials*. Eds.: M.A. Meyers, L.E. Murr and K.P. Staudhammer. Marcel Dekker, Inc., New York, 1023-1030.

Brar, N.S., Rosenberg, Z., and Bless, S.J. (1991). Spall strength and failure wave in glass. *J. de Physique IV, Coll. C3, Suppl. au. J. de Physique III*, 1, C3-639-644.

Brar, N.S., Rosenberg, Z., and Bless, S.J. (1992). Applying Steinberg model to the Hugoniot elastic limit of porous boron carbide specimens. In: *Shock Compression of Condensed Matter 1991*. Eds.: S.C. Schmidt, R.D.Dick, J.W.Forbes and D.G. Tasker. Els. Sc. Publ. B.V., 467-470.

Cagnoux, J. (1990). Spherical waves in pure alumina. Effect of grain size on flow and fracture. In: *Shock Compression of Condensed Matter 1989*. Eds.: S.C. Schmidt, J.N. Johnson and L.W. Davison. Els. Sc. Publ. B.V., 445-448.

Cagnoux, J. and Longy, F. (1988). Is the dynamic strength of alumina rate-dependent? In: *Shock Waves in Condensed Matter 1987*. Eds.: S.C. Schmidt and N.C. Holmes. Elsevier Science Publishers B.V., 293-296.

Chhabildas, L.C., Furnish, M.D., Reinhart, W.D., and Grady, D.E. (1998). Impact of AD995 alumina rods. In: *CP429, Shock Compression of Condensed Matter – 1997*. Eds.: S.C. Schmidt, D.P. Dandekar and J.W. Forbes. *AIP Conference Proceedings*, 429, 505-508.

Chan, H.M. and Lawn, B.R. (1988). Indentation deformation and fracture of sapphire. *J. Ceram. Soc.*, 71(1), 29-35.

Chandrasekar, S. and Chaudhri, M.M. (1994). The explosive desintegration of Prince Rupert's drops. *Philosophical Magazine*, 70(6), 1195-1218.

Christensen, R.J., Swanson S.R., and Brown, W.S. (1972). Split Hopkinson bar tests on rock under confining pressure. *Experimental Mechanics*, 12, 508-513.

Costin, L.S. (1983). A microcrack model for the deformation and failure of brittle rock. *J. Geophys. Res.*, 88(B11), 9485-9492.

Dandekar, D.P. (1994). Response of ceramics under shock wave loading. In: *High-Pressure Science and Technology - 1993*. Eds.: S.C. Schmidt, J.W. Shaner, G.A. Samara and M. Ross. *AIP Conference Proceedings*, 309, 729-732.

Dandekar, D.P. (1994). Shear strengths of aluminum nitride and titanium diboride under plane shock wave compression. *Journal de Physique IV*, 4, C8-379-384.

Dandekar, D.P. and Bartkowski, P. (1994). Shock response of AD995 alumina. In: *High-Pressure Science and Technology - 1993*. Eds.: S.C. Schmidt, J.W. Shaner, G.A. Samara and M. Ross. *AIP Conference Proceedings*, 309, 733-736.

Dandekar, D.P. and Beaulieu, P.A. (1995). Failure wave under shock wave compression in soda lime glass. In: *Metallurgical and Material Applications of Shock-Wave and High-Strain-Rate Phenomena*. Eds: L.E. Murr, K.P. Staudhammer, and M.A. Meyers. Elsevier Science B.V., 211-218.

Dandekar, D.P. and Gaeta, P.J. (1992). Extent of damage induced in titanium diboride under shock loading. In: *Shock-Wave and High-Strain-Rate Phenomena in Materials*. Eds.: M.A. Meyers, L.E. Murr and K.P. Staudhammer. Marcel Dekker, Inc., New York, 1059-1068.

Ernsberger, F.M. (1968). Role of densification in deformation of glasses under point loading. *J. Amer. Ceram. Soc.*, 51(10), 545-547.

Espinosa, H.D., Xu, Y., and Brar, N.S. (1977). Micromechanics of failure waves in glass. Part I: experiments. *J. Am. Cer. Soc.*, 80(8), 2061-2073.

Ewart, L. and Dandekar, D.P. (1994). Relationship between the shock response and microstructural features of titanium diboride (TiB_2). In: *High-Pressure Science and Technology - 1993*. Eds.: S.C. Schmidt, J.W. Shaner, G.A. Samara and M. Ross. *AIP Conference Proceedings*, 309, 1201-1204.

Feng, R., Gupta, Y.M., and Wong, M.K.W. (1997). Dynamic analysis of the response of lateral piezoresistance gauges in shocked ceramics. *J. Appl. Phys.*, 82(6), 2845-2854.

Feng, R., Gupta, Y.M., and Yuan, G. (1998). Dynamic strength and inelastic deformation of ceramics under shock wave loading. In: *CP429, Shock Compression of Condensed Matter – 1997*. Eds.: S.C. Schmidt, D.P. Dandekar and J.W. Forbes. *AIP Conference Proceedings*, 429, 483-488.

Feng, R., Raise, G.F., and Gupta, Y.M. (1996). Shock response of polycrystalline silicon carbide undergoing inelastic deformation. *J. Appl. Phys.*, 79(3), 1378-1386.

Feng, R. (2000). Formation and propagation of failure in shocked glasses, *J. Appl. Phys.* 87(4), 1693-1700.

Franklin, J.A. (1970). Triaxial strength of rock materials. *Rock Mechanics*, 3, 86-98.

Furnish, M.D. and Chhabildas, L.C. (1998). Alumina strength degradation in the elastic regime. In: *CP429, Shock Compression of Condensed Matter – 1997*. Eds.: S.C. Schmidt, D.P. Dandekar and J.W. Forbes. *AIP Conference Proceedings*, 429, 501-504.

Furnish, M.D., Grady, D.E., and Brown, J.M. (1986). Analysis of shock wave structure in single crystal olivine using VISAR. In: *Shock Waves in Condensed Matter – 1985*. Ed. Y.M. Gupta. Plenum Publishing Corp., New York, 595-600.

Galin, L.A., Ryabov, V.A., Fedoseev, D.V., and Cherepanov, G.I. (1966). On failure of a high-strength glass. *Dokl. AN SSSR*, **169**(5), 1034-1036. (In Russian.)

Galin, L.A. and Cherepanov, G.I. (1966). On self-supporting failure of a stressed brittle solid. *Dokl. AN SSSR*, **167**(3), 543-546. (In Russian.)

Glenn, L.A. and Janach, W. (1977). Failure of granite cylinders under impact loading. *Int. Journ. of Fracture*, **13**(3), 301-317.

Glenn, L.A. and Janach, W. (1978). Contrasting fracture models for granite under dynamic loading. *Trans. ASME: J. of Engineering Materials and Technology*, **100**, 287-293.

Grady, D.E. (1980). Shock deformation of brittle solids. *J. Geophys. Res.*, **85**(B2), 913.

Grady, D.E. (1985). The mechanics of fracture under high-rate stress loading. In: *Mechanics of Geomaterials*. Ed: Z. Bazant. J. Wiley & Sons Ltd., 129-156.

Grady, D.E. (1988). The spall strength of condensed matter. *J. Mech. Phys. Solids*, **36**(3), 353-384.

Grady, D.E. (1992). Shock-wave properties of high-strength ceramics. In: *Shock Compression of Condensed Matter 1991*. Eds.: S.C. Schmidt, R.D. Dick, J.W. Forbes and D.G. Tasker. Els. Sc. Publ. B.V., 455-458.

Grady, D.E. (1994). Impact strength and indentation hardness of high-strength ceramics. In: *High-Pressure Science and Technology - 1993*. Eds.: S.C.Schmidt, J.W.Shaner, G.A.Samara and M.Ross. *AIP Conference Proceedings*, **309**, 741-744.

Grady, D.E. (1994). Shock-wave strength properties of boron carbide and silicon carbide. *Journal de Physique IV*, **4**, C8-385-391.

Grady, D.E. (1998). Shock wave compression of brittle solids. *Mechanics of Materials*, **29**, 181-203.

Graham, R.A. (1974). Shock-wave compression of X-cut quartz as determined by electrical response measurements. *J.Phys. Chem. Solids*, **35**(3), 355-372.

Graham, R.A. (1993). Solids under High-Pressure Shock Compression. *Springer-Verlag*.

Graham, R.A. and Asay, J.R. (1978). *High Temp. High Press.*, **10**, 355.

Graham, R.A. and Ahrens, T.J. (1973). Shock wave compression of iron-silicate garnet. *J. Geophys. Res.*, **78**(2), 375-392.

Graham, R.A. and Brooks, W.P. (1971). Shock-wave compression of sapphire from 15 to 420 kbar. The effects of large anisotropic compression. *J. Phys. Chem. Solids*, **32**, 2311-2330.

Grouch, S.L. (1970) Experimental determination of volumetric strains in failed rock. *Int. J. Rock Mech. Min. Sci.*, **7**, 589-603.

Gust, W.H., Holt, A.C., and Royce, E.B. (1969). Dynamic yield, compressional, and elastic parameters for several lightweight intermetallic compounds. *J. Appl. Phys.* **44**(2), 550-560.

Gust, W.H. and Royce, E.B. (1971). Dynamic yield strength of B_4C, BeO, and Al_2O_3 ceramics. *J. Appl. Phys.* **42**, 276-295.

Hagan, J.T. (1980). Shear deformation under pyramidal indentations in soda-lime glass. *J. Mat. Sci.* **15**, 1417-1424.

Heard, H.C. and Cline, C.F. (1980). Mechanical behavior of polycrystalline BeO, Al_2O_3, and AIN at high pressure. *J. Mat. Sci.*, **15**, 1889-1897.

Hockey, B.J. (1971). Plastic deformation of aluminum oxide by indentation and abrasion. *J. Amer. Ceram. Soc.*, **54**, 223-231.

Holcomb, D.J. (1978). A quantitative model of dilatancy in dry rock and its application to Westerly granite. *J. Geophys. Res.*, **83**(B10), 4941-4950.

Holcomb, D.J. and Stevens, J.L. (1980). The reversible Griffith crack: a viable model for dilatancy. *J. Geophys. Res.* **85**(B12), 7101-7107.

Hopkinson, B. (1914). A Method of Measuring the Pressure Produced in Detonation of High Explosives or by Impact of Bullets. *Proc. Roy. Soc.*, **213A**, 437-456.

Horii, H. and Nemat-Nasser, S. (1985). Compression-induced macrocrack growth in brittle solids: axial splitting and shear failure. *J. Geophys. Res.*, **90**(B4), 3105-3125.

Janach, W. (1976). The role of bulking in brittle failure of rocks under rapid compression. *Int. Journal of Rock. Mech. Min. Sci. & Geomech. Abstr.*, **13**, 177-186.

Kanel, G.I. and Molodets, A.M. (1976). Behavior of the K8 glass under dynamic compression and following unloading. *Sov. Phys. - Tech. Phys.*, **XLVI** (2), 398-407.

Kanel, G.I., Molodets, A.M., and Dremin, A.N. (1977). Investigations of features of deforming a glass in intense. compression waves. *Phys. of Combustions and Explosions (USSR)*, **13**(6), 905-912. (In Russian).

Kanel, G.I. and Pityulin, A.N. (1984). *Phys. of Combustions and Explosions (USSR)*, **4**, 85.

Kanel, G.I., Razorenov, S.V., and Fortov, V.E. (1992). The failure waves and spallation in homogeneous brittle materials. In: *Shock Compression of Condensed Matter 1991*. Eds.: S.C. Schmidt, R.D. Dick, J.W. Forbes and D.G. Tasker. *Els.Sci.Publ.B.V.*, 451-454.

Kanel, G.I., Razorenov, S.V., Utkin, A.V., Baumung, K., Karow, H.U., and Licht, V. (1994). Spallations near the ultimate strength of solids. In: *High-Pressure Science and Technology - 1993*. Eds.: S.C. Schmidt, J.W. Shaner, G.A. Samara and M. Ross. *AIP Conference Proceedings, 309*, 1043-1046.

Kanel, G.I., Razorenov, S.V., Utkin, A.V., and Fortov, V.E. (1996). Shock-Wave Phenomena in Condensed Medias. *"Yanus-K", Moscow*. (In Russian.)

Kanel, G.I., Razorenov, S.V., Utkin, A.V., He, H., Jing, F., and Jin, X. (1998). Influence of the load conditions on the failure wave in glasses. *High Pressure Research, 16*, 27-44.

Kanel, G.I., Razorenov, S.V., Utkin, A.V., Dudin, S.N., Mintsev, V.B., Bless, S., and Simha, C.H.M. (1998). Investigation of mechanical properties of ceramics using axi-symmetric shock waves. in: *Shock Compression of Condensed Matter – 1997*. Eds.: S.C. Schmidt, D.D. Dandekar and J.W. Forbes. *AIP Conference Proceedings, 429*, 489-492.

Kipp, M.E. and Grady, D.E. (1990). Shock compression and release in high-strength ceramics. In: *Shock Compression of Condensed Matter 1989*. Eds.: S.C. Schmidt, J.N. Johnson and L.W. Davison. Els. Sc. Publ. B.V., 377-380.

Kipp, M.E. and Grady, D.E. (1992). Elastic wave dispersion in high-strength ceramics. In: *Shock Compression of Condensed Matter 1991*. Eds.: S.C. Schmidt, R.D. Dick, J.W. Forbes and D.G. Tasker. Els. Sc. Publ. B.V., 459-462.

Kolsky, H. and Shi, Y.Y. (1958). *Proc. Phys. Soc., London, 72*, 447.

Kranz, R.L. (1983). Microcracks in rocks: a review. *Tectonophysics, 100*, 449-480.

Kurita, K. and Fujii, N. (1979). Stress memory of crystalline rock in acoustic emission. *Geophys. Res. Lett. 6*, 9-12.

Lankford, J., Predebon, W.W., Staehler, J.M., Subhash, G., Pletka, B.J., and Anderson, C.E. (1998). The role of plasticity as a limiting factor in the compressive failure of high strength ceramics. *Mechanics of Materials, 29*, 205-218.

Longy, F. and Cagnoux, J. (1989). Plasticity and microcracking in shock-loaded alumina. *J. Amer. Ceram. Soc., 72*(6), 971-979.

Louro, L.H.L. and Meyers, M.A. (1989). Effect of stress state and microstructural parameters on impact damage of alumina-based ceramics. *J. Mat. Sci., 24*, 2516-2532.

Mashimo, T., Hanaoka, Y., and Nagayama, K. (1988). Elastoplastic properties under shock compression of Al_2O_3 single crystal and polycrystal. *J. Appl. Phys., 63*(2), 327-336.

Mashimo, T., and Uchino, M. (1997). Heterogeneous free-surface profile of B_4C polycrystal under shock compression. *J. Appl. Phys., 81*(10), 7064-7065.

McClintock, F.A. and Argon, A.S. (1966). *Mechanical behavior of materials*. Addison-Wesley Publ.

Me-Bar, Y., Boas, M., and Rosenberg, Z. (1987). *Mat. Sci. Eng., 85*, 77.

Morris, C.E. (Ed.) (1982). Los Alamos Shock Wave Profile data. University of California Press.

Moss, W.C. and Gupta, Y.M. (1982). A constitutive model describing dilatancy and cracking in brittle materials. *J. Geophys. Res., 87*(B4), 2985-2998.

Munson, D.E. and Lawrence, R.J. (1979). Dynamic deformation of polycrystalline alumina. *J. Appl. Phys., 50*(10), 6272-6282.

Murray, N.H., Bourne, N.K., and Rosenberg, Z. (1996). Precursor decay in several aluminas. In: *Shock Compression of Condensed Matter - 1995*. Eds.: S.C. Schmidt and W.C. Tao. *AIP Conference Proceedings 370*, 491-494.

Nahme, H., Hohler, V., and Stilp, A. (1994). Determination of the dynamic material properties of shock loaded silicon nitride. In: *High-Pressure Science and Technology - 1993*. Eds.: S.C. Schmidt, J.W. Shaner, G.A. Samara and M. Ross. *AIP Conference Proceedings, 309*, 765-768.

Nemat-Nasser, S. and Horii, H. (1982). Compression-induced nonplanar crack extension with application to splitting, exfoliation, and rockburst. *J. Geophys. Res., 87*(B8), 6805-6821.

Nemat-Nasser, S. and Obate, M. (1988). A microcrack model of dilatancy in brittle materials. *Trans. ASME: J. Appl. Mech., 55*(110), 24-35.

Pickup, I.M. and Barker, A.K. (1998). Damage kinetics in silicone carbide. In: *Shock Compression of Condensed Matter – 1997*. Eds.: S.C. Schmidt, D.D. Dandekar and J.W. Forbes. *AIP Conference Proceedings, 429*, 513-516.

Raiser, G. and Clifton, R.J. (1994). Failure Waves in Uniaxial Compression of an Aluminosilicate Glass. In: *High-Pressure Science and Technology - 1993*. Eds.: S.C. Schmidt, J.W. Shaner, G.A. Samara and M.Ross. *AIP Conference Proceedings, 309*, 1039-1042.

Raiser, G., Wise, J.L., Clifton, R.J., Grady, D.E., and Cox, D.E. (1994). Plate impact response of ceramics and glasses. *J. Appl. Phys., 75*(8), 3862-3869.

Razorenov, S.V., Kanel, G.I., Fortov, V.E., and Abasehov, M.M. (1991). The fracture of glass under high-pressure impulsive loading. *High Pressure Research, 6*, 225-232.

Razorenov, S.V., Kanel, G.I., and Yalovets, T.N. (1993). Dynamic strength of ruby. *J. Chem. Phys.* (USSR).

Razorenov, S.V., Bogatch, A.A., Kanel, G.I., Utkin, A.V., Fortov, V.E., and Grady, D.E. (1998). Elastic-Plastic Deformation and Spall Fracture of Metals at High Temperatures. In: *Shock Compression of Condensed Matter – 1997*. Eds.: S.C. Schmidt, D.D. Dandekar and J.W. Forbes. *AIP Conference Proceedings,* **429**, 447-480.

Romanchenko, V.I. and Stepanov, G.V. (1980). *J. Appl. Mech. Tech. Phys.*, **21**(4), 141.

Rosenberg, Z. (1987). *J. Appl. Phys.*, **62**(5), 1745.

Rosenberg, Z. (1992). The response of ceramic materials to shock loading. In: *Shock Compression of Condensed Matter 1991*. Eds.: S.C. Schmidt, R.D. Dick, J.W. Forbes and D.G. Tasker. Els. Sc. Publ. B.V., 439-444.

Rosenberg, Z. (1993). On the relation between the Hugoniot elastic limit and the yield strength of brittle materials. *J. Appl. Phys.*, **73**(12).

Rosenberg, Z. (1994). On the shear strength of shock loaded brittle solids. *J. Appl. Phys.*, **76**(3), 1543-1546.

Rosenberg, Z., Brar, N.S. and Bless, S.J. (1992). Shear strength of titanium diboride under shock loading measured by transverse manganin gauges. In: *Shock Compression of Condensed Matter 1991*. Eds.: S.C. Schmidt, R.D. Dick, J.W. Forbes and D.G. Tasker. Els. Sc. Publ. B.V., 471-473.

Schmitt, D., Svendsen, B. and Ahrens, T.J. (1986). Shock induced radiation from minerals. In: *Shock Waves in Condensed Matter – 1985*. Ed.: Y.M. Gupta. Plenum Publishing Corp., New York, 261-265.

Scholz, C.H. (1968). Experimental study of the fracturing process in brittle rock. *J. Geophys. Res.*, **73**, 1447-1454.

Seaman, L., Curran, D.R., and Shockey, D.A. (1976). *J. Appl. Phys.*, **47**, 4814.

Senf, H., Strassburger, E., and Rothenhausler H. (1995). Visualization of fracture nucleation during impact in glass. In: *Metallurgical and Material Applications of Shock-Wave and High-Strain-Rate Phenomena*. Eds: L.E. Murr, K.P. Staudhammer and M.A. Meyers. Elsevier Science B.V., 163-170.

Schardin, H. (1959). Velocity effects in fracture. In: *Fracture*. Eds: B.L. Averbach et al. MIT Press, Cambridge, Mass., and Wiley, New York, 297-330.

Simha, H. (1999). (2000). High rate loading of a high-purity ceramic: One-dimensional stress experiments and constitutive modeling. (Thesis). In: *DAI-B 60/07*, 3361. The University of Texas at Austin.

Song, H., Bless, S.J., Brar, N.S., Simha, C.H., and Jang, S.D. (1994). In: *High-Pressure Science and Technology - 1993*. Eds.: S.C. Schmidt, J.W. Shaner, G.A. Samara and M. Ross. *AIP Conference Proceedings,* **309**, 737-740.

Staehler, J.M., Predeborn, W.W., and Pletka, B.J. (1994). The response of a high-purity alumina to plate-impact testing. In: *High-Pressure Science and Technology - 1993*. Eds.: S.C. Schmidt, J.W. Shaner, G.A. Samara and M. Ross. *AIP Conference Proceedings,* **309**, 745-748.

Stevens, J.L. and Holkomb, D.J. (1980). A theoretical investigation of the sliding crack model of dilatancy. *J. Geophys. Res.*, **85**(B12), 7091-7100.

Sugiure, S.H., Kondo, K., and Sawaoka, A. (1981). Dynamic response of fused quartz in the permanent densification region. *J. Appl. Phys.*, **52**(5), 3375-3382.

Swegle, J.W. and Grady, D.E. (1985). Shock viscosity and the prediction of shock wave rise times. *J. Appl. Phys.*, **58**, 692-701.

Tranchet, J-Y. and Collombet, F. (1995). Behavior of a pure alumina submitted to a divergent spherical stress wave. In: *Metallurgical Applications of Shock-Wave and High-Strain-Rate Phenomena*. Eds.: L.E. Murr, K.P. Staudhammer and M.A. Meyers. *Els. Science B.V.*, 535-542.

Tapponier, R. and Brace, W.F. (1976). Development of stress-induced microcracks in Westerly granite. *Int. J. Rock Mech. Min. Sci. Geomech. Abstr.*, **13**, 103-112.

Wackerle, J. (1962). *J. Appl. Phys.*, **33**, 922.

Wang, Y. and Mikkola, D.E. (1992). Response of alpha-aluminum oxide to shock impact. In: *Shock-Wave and High-Strain-Rate Phenomena in Materials*. Eds.: M.A. Meyers, L.E. Murr and K.P. Staudhammer. Marcel Dekker, Inc., New York, 1031-1040.

Wawersik, W.R. and Brace, W.F. (1971). Post-failure behavior of a granite and diabase. *Rock Mechanics*, **3**, 61-85.

Winkler, W.-D. and Stilp, A.J. (1992). Spallation behavior of the TiB_2, SiC, and B_4C under planar impact tensile stresses. In: *Shock Compression of Condensed Matter 1991*. Eds.: S.C. Schmidt, R.D. Dick, J.W. Forbes and D.G. Tasker. Els. Sc. Publ. B.V., 475-478.

Winkler, W.-D. and Stilp, A.J. (1992). Pressure induced macro- and micromechanical phenomena in planar impacted TiB_2. In: *Shock Compression of Condensed Matter 1991*. Eds.: S.C. Schmidt, R.D. Dick, J.W. Forbes and D.G. Tasker. Els. Sc. Publ. B.V., 555-558.

Wise, J.L. and Grady, D.E. (1994). Dynamic, multiaxial impact response of confined and unconfined ceramic rods. In: *High-Pressure Science and Technology - 1993*. Eds.: S.C. Schmidt, J.W. Shaner, G.A. Samara and M. Ross. *AIP Conference Proceedings,* **309**, 777-780.

Yaziv, D., Yeshurun, Y., Partom, Y., and Rosenberg, Z. (1988). Shock structure and precursor decay in commercial alumina. In: *Shock Compression of Condensed Matter 1987*. Eds.: S.C. Schmidt and N.C. Holmes. Els. Sc. Publ. B.V., 297-300.

Zel'dovich, Ya.B. and Raizer, Yu.P. (1967). *Physics of Shock Waves and High-Temperature Hydrodynamic Phenomena*, Academic Press, New York.

Distribution List

Administrator
Defense Technical Information Center
ATTN: DTIC-DDA
8725 John J. Kingman Road,
Ste 0944
Ft. Belvoir, VA 22060-6218

Tim Holmquist
U.S. Army High Performance Computing Re
1200 Washington Avenue S
Minneapolis, MN 55415

Naury Birnbaum
President
Century Dynamics, Inc.
2333 San Ramon Valley Blvd
Suite 185
San Ramon, CA 945831613

Dr. Joe Foster
Air Force Armament & Technology Lab
AFATL/MNW
Eglin AFB, FL 32542

Dr. Gordon Johnson
Alliant Techsystems, Inc.
Marine Systems Division
MN-11-2925
600 Second St. NE
Hopkins, MN 55343

Marc Adams
Jet Propulsion Laboratory
Impact Physics Group
4800 Oak Grove Dr.
Pasadena, CA 91109

Dr. Charles Anderson, Jr.
Southwest Research Institute
6220 Culebra Rd.
P. O. Drawer 28510
San Antonio, TX 78284

Director
U.S. Army Research Lab
ATTN: AMSRL OP SD TA
2800 Powder Mill Road
Adelphi, MD 20783-1145

Thomas J. Ahrens
CALTECH 252-21
Pasadena, CA 91125

Dr. Dennis L. Orphal
International Research Associates
4450 Black Ave., Suite E
Pleasanton, CA 94566

Director
U.S. Army Research Lab
ATTN: AMSRL OP SD TL
2800 Powder Mill Road
Adelphi, MD 20783-1145

Dr. Lalit C. Chhabildas
Sandia National Labs
Experimental Impact Physics
Dept. 1433
MS 0821
Albuquerque, NM 87185-1187

Mr. William Flis
Dyna East Corporation
3620 Horizon Drive
King of Prussia, PA 19406-2647

Director
U.S. Army Research Lab
ATTN: AMSRL OP SD TP
2800 Powder Mill Road
Adelphi, MD 20783-1145

Mr. William A. Gooch
US Army Research Laboratory
ATTN: AMSRL-WT-TA
Aberdeen Prvg Grd, MD 21005-5066

Dr. V. Hohler
Ernst Mach Institute
Eckerstrasse 4
D-79104 Frieburg
GERMANY

Dr. Bruce Burns
U.S Army Research Laboratory
ATTN: AMSRL-WT-PD
Bldg. 390
Aberdeen Prvg Grd, MD 21005-5066

Dennis Grady
Applied Research Associates, Inc.
4300 San Mateo Blvd NE, Suite A220
Albuquerque, NM 87110

Dr. W. J. Gillich
U.S. Army Research Laboratory
AMSRL-WT-TA
Aberdeen Prvg Grd, MD 21005-5066

Army Research Laboratory
AMSRL-CI-LP
Technical Library 305
Aberdeen Prvg Grd, MD 21005-5066

Mr. Nick Lynch
DERA Fort Halstead
Bldg. A 20, Div. WX5
Sevenoaks, Kent
TN14 7BP
ENGLAND

Distribution List

Dr. A. M. Rajendran
U.S. Army Research Office
P. O. Box 12211
Research Triangle Park, NC 27709

Dr. Michael Normandia
U.S. Army Research Laboratory
ATTN: AMSRL-WM-TA
Aberdeen Prvg Grd, MD 21005-5066

Lewis Glenn
Lawrence Livermore National Laboratory
Box 808, L-200
Livermore, CA 94550

J.Y. Tranchet
Centre d'Etudes de Gramat
46500 Gramat
FRANCE

Hari Simha
University of Dayton Research Institute
Impact Physics Laboratory
300 College Park
Dayton, OH 45469-0182

R. Feng
Engineering Mechanics
University of Nebraska-Lincoln
Lincoln, NE 68588-0526

Gennady Kanel
Institute for Chemical Physics Research
Chernogolovka
Moscow r-n
142432
RUSSIA

Philip M. Cunniff
U.S. Army Soldier Systems Center
ATTN: AMSSB-RIP-B(N)
Kansas Street
Natick, MA 01760-5019

Dr. James McCauley
U.S. Army Research Laboratory
ATTN: AMSRL-WM-M
(Bldg. 4600)
Aberdeen Proving Ground, MD 21005-5066

Rodney J. Clifton
Brown University
Box D, BU
Providence, RI 02912-1844

Patrik Lundberg
FOA - Defense Research Establishment
Gindsjon
S-14725 Tumba
Sweden

Lothar W. Meyer
Technical University Chemnitz
Fak. MBVT-24300-
D-09107 Chemnitz
GERMANY

Anatoli Kozhushko
Russian Academy of Sciences
Ioffe Physical Technical Institute
Hypervelocity Impact Research Group
St. Petersburg
194021
RUSSIA

Doug Templeton
U.S. Army Tank Automotive Command
Attn: AMSTA-TR-R, MS 263
Warren, MI 48797-5000

Eugene Zaretsky
Department of Mechanical Engineering
Ben Gurion University of the Negev
PO BOX 653
Beer-Sheva 84105
ISRAEL

Valeriy V. Kartuzov
National Academy of Sciences of Ukraine
Frantzevich Institute for Problems of
Materials Science
Department 44
3, Krzhyzhanovsky Str.
252142, Kiev, Ukraine

Francois Hild
Laboratoire de Mecanique et Technolgie
61 avenue du President Wilson
94 235 Cachan cedex
France

Prof. Janusz Klepaczko
Laboratory of Physics and Mechanics of Mate
Metz University
Ile du Saulcy
BP80794
F-57012
Metz Cedex 01
FRANCE

V. F. Nesterenko
3175-C Evening Way
La Jolla, CA 92037

Neil Bourne
University of Cambridge
Cavendish Laboratories
Madingley Road
Cambridge CB3 OHE
UK